Electronic and Vibrational Properties of Fluorenone in the Channels of Zeolite L

André Devaux, Claudia Minkowski, and Gion Calzaferri*[a]

Abstract: Fluorenone ($C_{13}H_8O$) was inserted into the channels of zeolite L by using gas-phase adsorption. The size, structure, and stability of fluorenone are well suited for studying host–guest interactions. The Fourier transform IR, Raman, luminescence, and excitation spectra, in addition to thermal analysis data, of fluorenone in solution and fluorenone/zeolite L are reported. Normal coordinate analysis of fluorenone was performed, based on which IR and Raman bands were assigned, and an experimental force field was determined. The vibrational spectra can be used for nondestructive quantitative analysis by comparing a characteristic dye band with a zeolite band that has been chosen as the internal standard. Molecular orbital calculations were performed to gain a better understanding of the electronic structure of the system and to support the interpretation of the electronic absorption and luminescence spectra. Fluorenone shows unusual luminescence behavior in that it emits from two states. The relative intensity of these two bands depends strongly on the environment and changes unexpectedly in response to temperature. In fluorenone/zeolite L, the intensity of the 300 nm band (lifetime 9 μs) increases with decreasing temperature, while the opposite is true for the 400 nm band (lifetime 115 μs). A model of the host–guest interaction is derived from the experimental results and calculations: the dye molecule sits close to the channel walls with the carbonyl group pointing to an Al^{3+} site of the zeolite framework. A secondary interaction was observed between the fluorenone's aromatic ring and the zeolite's charge-compensating cations.

Keywords: fluorenone · host–guest systems · luminescence · normal coordinate analysis · vibrational spectroscopy · zeolites

Introduction

A fascinating quality of photochemistry is the design of artificial photonic antenna systems for light harvesting and transport, analogous to the photosynthesis in a plant leaf in which sunlight is absorbed and transported by the chlorophyll molecules to a reaction center where it is trapped and transformed into chemical energy. Such artificial systems are of great interest because they are capable of elaborating the energy information input of photons to perform useful functions, such as processing and storage of information, sensing the microscopic environment on a molecular level, or transformation and storage of solar energy. In natural antennae, the formation of aggregates is prevented by fencing in the chlorophyll molecules by means of polypeptides. One way to implement this in an artificial antenna is to choose a microporous material with cavities large enough to take up monomers of dye molecules, but not aggregates. Zeolite L with its one-dimensional tube structure is a very versatile host material. Each individual channel can be filled successively with joint and, in many cases, noninteracting dye molecules. The latter can be selectively excited with light. Depending on the structure of the material, the excitation energy can migrate through a directed transport route along the channel axis from the center of the crystal towards a target molecule at the entrance of the channel, or vice versa.[1] The chemical, photochemical, and photophysical properties of the dye–zeolite L host–guest materials are largely influenced by the geometrical constraints imposed by the host. They also depend on the presence of solvent molecules and co-cations. Co-adsorbed water plays an important role in many of these materials. It was observed that, for example, exposure of dry *p*-terphenyl/zeolite to air of 22% relative humidity at room temperature leads to a displacement of the *p*-terphenyl from the channels. Upon heating and hence drying the zeolite, the organic molecule can be inserted again. The removal and insertion process is reversible.[2] In contrast to this, incorporated fluorenone is

[a] Dr. A. Devaux, C. Minkowski, Prof. Dr. G. Calzaferri
Department of Chemistry and Biochemistry
University of Bern, Freiestrasse 3
3012 Bern (Switzerland)
Fax: (+41) 31-6313994
E-mail: gion.calzaferri@iac.unibe.ch

Supporting information for this article is available on the WWW under http://www.chemeurj.org/ or from the author. It contains Tables S1–S4 describing the symmetrized force fields used for the normal coordinate analyses.

 DOI: 10.1002/chem.200305673

not displaced by water molecules under ambient conditions, but remains inside the channels. The main difference between *p*-terphenyl and fluorenone, with respect to this property, is that the latter bears a carbonyl group. This observation played a major role in the selection and hence realization of the first stopcock fluorophore-dye/zeolite L material.[3] We now report the results obtained in a detailed study of fluorenone/zeolite L by means of luminescence, IR, and Raman spectroscopy, thermal analysis, and theoretical reasoning.

Background

Host: Zeolite L is a crystalline aluminosilicate with hexagonal symmetry. Its anionic framework and the position of the charge-compensating cations are illustrated in Figure 1. The crystals consist of cancrinite cages (ε-cages) connected by double 6-rings. These units form columns in the *c* direction that are connected, thus giving rise to 12-membered rings with a free diameter of 0.71 nm. As a consequence, zeolite L consists of one-dimensional channels running through the whole crystal, in which the largest free diameter is 1.26 nm and a unit cell (u.c.) length is 0.75 nm. The main channels are connected by nonplanar 8-rings with an opening of about 0.15 nm, forming an additional two-dimensional channel system. The scanning electron microscopy (SEM) picture in Figure 1e shows the hexagonal structure of the zeolite L material. Four different cation sites have been reported (Figure 1c): *A* is located in the center of the double 6-ring, while *B* lies in the center of the ε-cage. *C* is midway between the centers of two adjacent cancrinite cages, and *D* lies inside the main channel near the wall of the 8-ring. Dehydrated zeolite L shows an additional cation site (*E*) located midway between two adjacent *A* sites. Water molecules in the large cavities were reported to behave like an intracrystalline liquid, whereas they seem to build clusters around the cations in the smaller pores. Nearly all of the zeolite L water content can be removed at room temperature by applying a high vacuum (~10^{-5} mbar). The stoichiometry of zeolite L with monovalent cations (M) is $(M)_9[Al_9Si_{27}O_{72}]\cdot n\,H_2O$, in which *n* equals 21 in fully hydrated materials and 16 at about 22% relative humidity. The number of channels lying parallel to the *c* axis is equal to $0.265(d_c)^2$, in which d_c is the diameter of the cylinder in nm. As an example, a crystal with a diameter of 550 nm contains about 8×10^4 parallel channels.

Host–guest materials: Dye molecules are positioned at sites along the large, one-dimensional channels of zeolite L. The length of a site corresponds to a number *s* multiplied by the unit cell length, so that one dye molecule fits into one site. The value of *s* depends on the size of the molecule and the length of the primitive unit cell. A site can either be occupied by a dye molecule or it can be empty. Under equilibrium conditions, all sites can often be assumed to be equivalent and to have the same probability of being occupied by a dye molecule. The occupation probability (*p*) is equal to the ratio of the occupied sites to the total number of equivalent sites. For example, a zeolite L channel with a length of

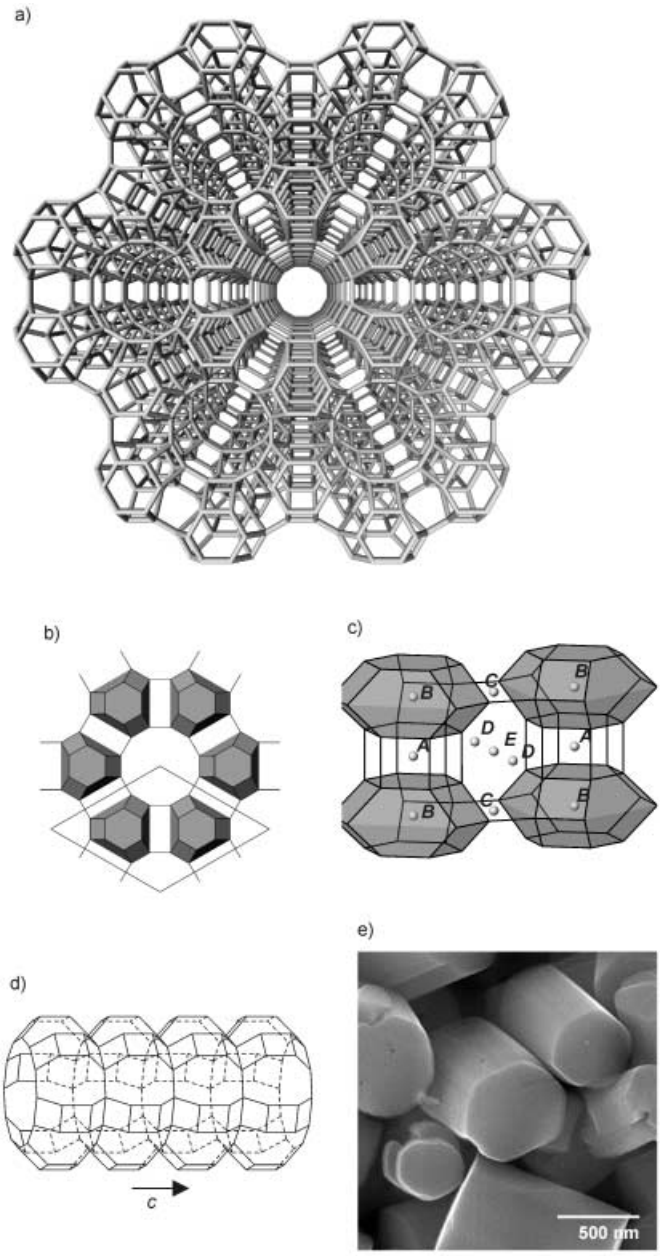

Figure 1. Zeolite L framework: a) projection along the *c* axis, b) cancrinite cages highlighted as polyhedra; c) section with the different cationic positions *A* to *E*; d) side view of the 12-ring channel along the *c* axis; e) SEM picture of zeolite L crystals.

700 nm contains 932 u.c., which also corresponds to the number of sites for a molecule the size of fluorenone. The total number of such sites per zeolite L crystal (700 nm in length and 550 nm in diameter) is $n_{tot}\approx64\times10^6$. The dye concentration $c(p)$ in mol L^{-1} in a zeolite L nanocrystal is related to *p* as shown in Equation (1):

$$c(p)=\frac{\rho_z}{Mm_z s}p \qquad (1)$$

in which ρ_z is the density of the zeolite nanocrystal (2.17 g cm^{-3}), Mm_z is the molecular mass of the unit cell (about 2883 g mol^{-1}), and *s* is the number of unit cells

needed for one site (equal to 1 for fluorenone). Using the numbers given in brackets we obtain Equation (2):

$$c(p) = (0.752\,\mathrm{mol\,L^{-1}})p \quad (2)$$

Neutral and cationic dyes of different structure have been inserted into zeolite L and remarkable photophysical observations have been reported. For recent reviews we refer to refs. [1,4,5].

Guest: The guest molecule we chose for our study is fluorenone ($C_{13}H_8O$). Its structure is displayed at the bottom of Figure 2, while the top shows two of the many possible orientations of fluorenone in a zeolite L channel. Channel diameters and molecular dimensions are based on van der Waals radii. The carbonyl group is the only functional group. Fluorenone is a planar molecule with C_{2v} symmetry, as confirmed by X-ray diffraction analysis.[6] Two different symmetry designations are possible as it can be placed either in the *xz* or *yz* plane. For our calculations the molecule was located in the *xz* plane (Zwarich et al.[21] placed it in the *yz* plane). Changing the orientation of the molecule from one plane to the other switches the designations of the B_1 and B_2 point group symbols. The size and the structure of fluorenone allow a reasonably easy treatment by normal coordinate analysis and molecular orbital (MO) calculations. Both fluorenone in solution and the fluorenone/zeolite L material are photostable. Fluorenone can be easily inserted into the channels of zeolite L due to its size, photochemical and thermal stability, and its low sublimation temperature (100 °C at 0.5 Torr). It has a nonalternant π-electron system and displays unusual spectroscopic and photophysical properties that have been extensively studied in solution. Assignment of states,[7] interpretation of solvent and concentration effects,[8] luminescence yields and lifetimes,[9,10] and laser flash-photolytic experiments[11] have been reported. The basic photophysical parameters of fluorenone and of some derivatives have been measured as a function of temperature in a variety of solvents.[12] The existence of delayed fluorescence in acetonitrile has been attributed to excimer formation by laser-induced fluorescence.[11] However, no excimer emission could be found in hexane, cyclohexane, and alcohols.[8,13,14] Correct assignment of the lowest singlet–singlet electronic absorption proved to be quite difficult.[15] Intensity considerations were not very helpful in this case, as the observed lowest energy transition is somewhat strong for an n–π* transition, but rather weak for a π–π* transition. The energy of the band is also quite low for an n–π* transition, but not low enough to rule out such an assignment. Solvent effects were more useful, in so far as this band is redshifted in polar solvents. Such shifts are characteristic for π–π* transitions. The most conclusive result for the assignment was the effect of oxime formation on the absorption spectra. It was shown that the formation of an oxime results in the disappearance of n–π* transitions associated with the carbonyl group, but has little influence on π–π* transitions. The long-wavelength absorption spectrum of fluorenone oxime is essentially the same as for fluorenone. The only difference is a slight blueshift of the maximum of the long-wavelength transition, with no change in the extinction coefficient. This result can be considered as final proof that the observed lowest energy electronic absorption has π–π* character.[15]

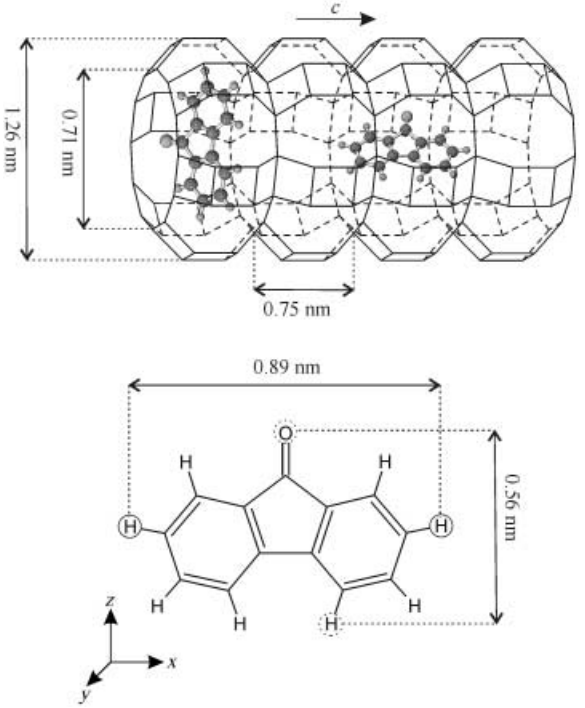

Figure 2. Top: two among many other possible orientations of fluorenone molecules in a zeolite L channel. Bottom: structure and dimensions of fluorenone. The channel diameters and molecular dimensions are based on van der Waals radii. The unit cell length is 0.75 nm.

Electronic transition dipole moment: The electronic transition dipole moment ($\vec{\mu}^{ed}_{nm}$) between two wave functions ψ_n and ψ_m is defined in Equation (3):

$$\vec{\mu}^{ed}_{nm} = \psi_n|-(\sum_i e\vec{r}_i)|\psi_m > \quad (3)$$

The oscillator strength (f) of the transition $n \leftarrow m$ is shown in Equation (4):

$$f = \frac{8\pi^2\tilde{\nu}cm_e}{3he^2}|\vec{\mu}^{ed}_{nm}|^2 \quad (4)$$

By making use of the definition of the square of the transition dipole length, $|D_{nm}|^2$ [Eq. (5)],

$$|D_{nm}|^2 = \frac{1}{e^2}|\vec{\mu}^{ed}_{nm}|^2 \quad (5)$$

we obtain Equation (6) [from substitution of Eq. (5) into Eq. (4)]:

$$f = l_0\tilde{\nu}|D_{nm}|^2 \quad (6)$$

in which e is the elementary charge, h is Planck's constant, m_e is the electron mass, c is the speed of light in a vacuum,

$\vec{r}_i$ are the electron position vectors, $\tilde{\nu}$ is the energy in cm^{-1} of the transition $n \leftarrow m$, and l_0 is equal to 1.085×10^{-5} cm Å^{-2}; f is a dimensionless quantity.[16,17]

Results

Fluorenone/zeolite L is a yellowish, moderately luminescent powder, with a more intense coloring for higher loading. The material displays very good photostability, because long exposure to light did not alter its spectroscopic properties in any way. X-ray powder diffraction analysis showed that the zeolite framework is not damaged during the synthesis of the host–guest system. To investigate the influence of co-adsorbed water on the dye location, fluorenone/zeolite L samples were suspended in 1-butanol. After centrifugation, the fluorenone concentration in the supernatant was determined spectrophotometrically. The amount of fluorenone inside the zeolite was determined by comparing the fluorenone content of the 1-butanol phase with the total amount of dye present in the sample. This experiment was performed with dry and rehydrated samples. In both cases, the quantity of fluorenone in the solvent was identical and corresponded typically to about 1% (wt) of the total amount of dye. The fluorenone loading of washed fluorenone/zeolite L samples, determined by dissolving the zeolite framework, was consistent with the results from the washing experiments. The quantity of fluorenone remaining in the channels of zeolite L was identical for both dry and rehydrated samples stemming from the same synthesis. These properties facilitate thermal analysis, UV-visible, fluorescence, and vibrational spectroscopy.

Thermal analysis: The thermal stability of rehydrated fluorenone/zeolite L samples was studied by means of thermogravimetric analysis (TGA) and differential scanning calorimetry (DSC), and the results were compared with those of unloaded zeolite L. Figure 3 shows the desorption (TGA) and its first derivative (DTG) curves as a function of temperature for A) hydrated zeolite L, B) the corresponding curves for fluorenone/zeolite L , and C) crystalline fluorenone. Hydrated zeolite L loses about 95% of its water content in a desorption step between 25 and 220°C. The remaining water leaves the zeolite at a much slower, continuous rate at higher temperatures. The maximum of the DTG peak appears at 110°C. This peak shifts to a lower temperature of about 100°C in the case of the fluorenone/zeolite L, an observation which is similar to that reported for *p*-terphenyl/zeolite L.[2] We observed two additional features, one at 500°C and the other at 680°C, which are due to the loss of fluorenone. The TGA of crystalline fluorenone exhibits a fast desorption step at 270°C. Figure 4 shows the DSC for both zeolite L and fluorenone/zeolite L. The zeolite L sample shows a sharp endothermic transition around 270°C, which can be attributed to water desorption from the zeolite.[18,19] This transition shifts to 250°C in the case of the fluorenone/zeolite L material. No additional changes could be observed.

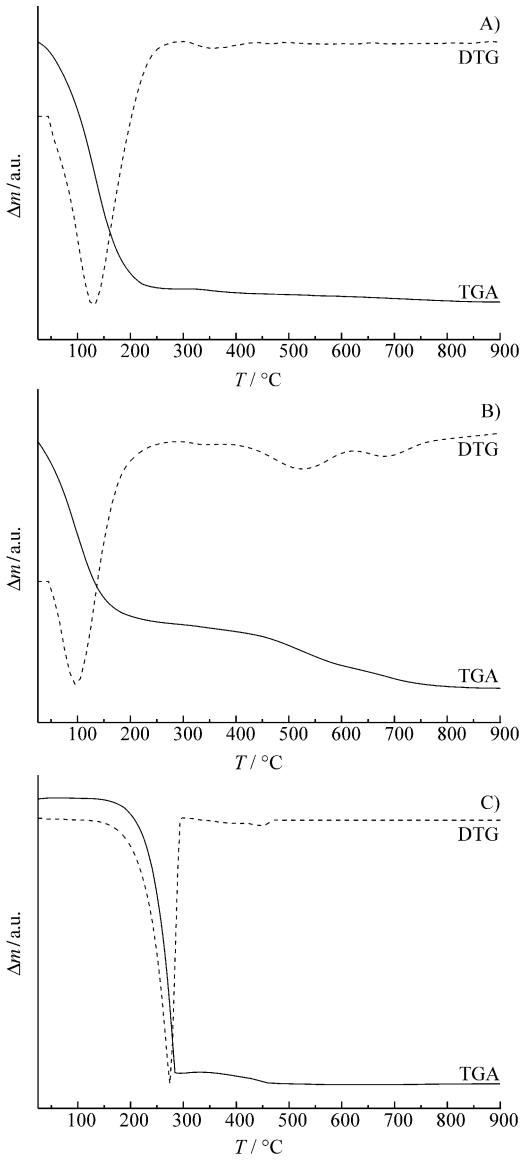

Figure 3. TGA and its derivative (DTG) of A) hydrated zeolite L, B) rehydrated fluorenone/zeolite L ($p = 0.2$), and C) crystalline fluorenone, observed at a heating rate of 5°C min^{-1} in a nitrogen stream of 15 mL min^{-1}.

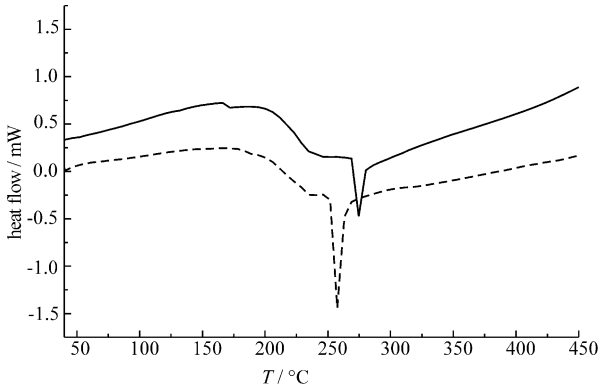

Figure 4. DSC of zeolite L (solid) and fluorenone/zeolite L (dashed) observed at a heating rate of 10°C min^{-1} in an N_2 stream of 80 mL min^{-1}.

Electronic spectroscopy

UV-visible spectra: The absorption spectrum of fluorenone in cyclohexane (10^{-5} M) is shown in Figure 5A) and the diffuse reflectance absorption spectrum of fluorenone/zeolite L is presented in B). The spectra are plotted on a logarithmic scale to visualize the weak, long-wavelength transitions. The spectrum in A) can be divided into three regions: the first contains a broad, weak band around 380 nm ($\varepsilon_{380}=430\,\mathrm{L\,mol^{-1}\,cm^{-1}}$). The second region, ranging from 320 to 260 nm ($\varepsilon_{292}=5.5\times10^3$, $\varepsilon_{282}=4.5\times10^3$, $\varepsilon_{305}=2.6\times10^3\,\mathrm{L\,mol^{-1}\,cm^{-1}}$), has a more intense and structured band system. The last region consists of two close-lying, strong peaks around 250 nm ($\varepsilon_{256}=1.0\times10^5$, $\varepsilon_{249}=8.0\times10^4\,\mathrm{L\,mol^{-1}\,cm^{-1}}$). The intensity of these two peaks is about 3 orders of magnitude higher than that of the 380 nm band. The spectrum of fluorenone/zeolite L displays a comparable band structure and intensity distribution, but with broader peaks. Similar spectra to those in A) were reported and discussed in refs. [7,10,15]. A complete assignment of the absorption spectrum, based on spectra in different solvents and MO calculations, was carried out by Kuboyama.[7] The two peaks at 250 nm can be considered a vibrational structure belonging to a single π–π* transition ($^1B_1\leftarrow{}^1A_1$), with a hidden transition ($^1A_1\leftarrow{}^1A_1$) on the longer wavelength side. The 290 nm band is assigned to an $^1A_1\leftarrow{}^1A_1$ transition, and the 310 nm and 380 nm bands to $^1B_1\leftarrow{}^1A_1$ transitions. All these transitions are of π–π* type. This means that the spectrum shown in Figure 5A) is well understood.

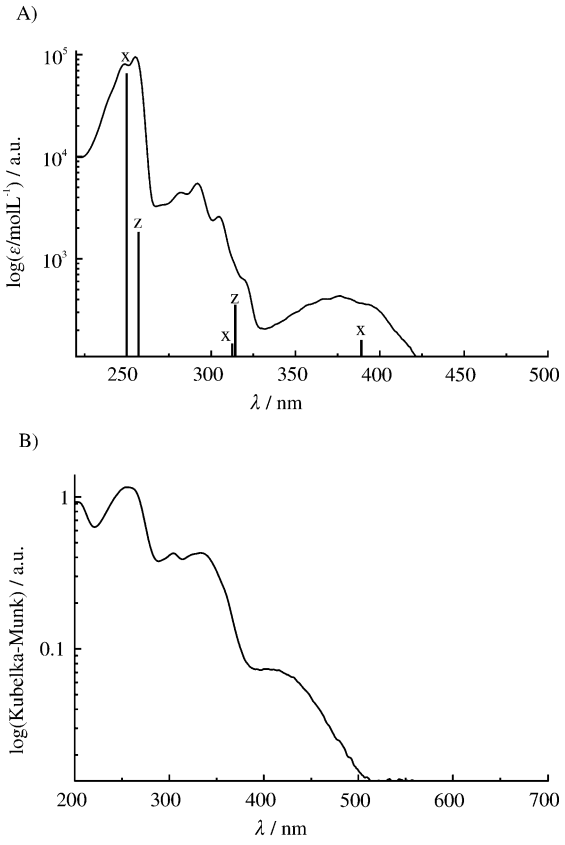

Figure 5. A) Electronic absorption spectrum of a 10^{-5} M solution of fluorenone in cyclohexane at room temperature. Calculated electronic transitions are indicated as lines. Their polarization is identified by a letter (x = *x* polarized, z = *z* polarized). B) Diffuse reflectance absorption spectrum of a fluorenone/zeolite L sample ($p=0.3$).

Luminescence spectra: The emission spectra of fluorenone in solution were recorded in the presence and absence of oxygen at room temperature. Luminescence spectra of fluorenone/zeolite L were measured in the presence of oxygen at different temperatures. Spectra measured at room temperature are displayed in Figure 6. The excitation wavelength was 250 nm for fluorenone/zeolite L and 270 nm for fluorenone in solution. These values were chosen in order to correspond to the most intense absorption band for each case. The spectrum of the fluorenone/zeolite L displays a sharp peak at 300 nm and an intense, broader band at 400 nm. The spectrum of fluorenone in cyclohexane consists of an intense peak at 310 nm and of a broad, weak band at 470 nm. The emission spectrum is identical for degassed and non-degassed solutions. The bands of the fluorenone/zeolite L sample appear at higher energy relative to those of fluorenone in cyclohexane, with the lower energy band undergoing a large shift of about 3100 $\mathrm{cm^{-1}}$. The higher energy band shifts by 1000 $\mathrm{cm^{-1}}$. The relative intensities of the emissions are quite different: the most intense band in solution lies at 310 nm, whereas in the fluorenone/zeolite L sample the band at 400 nm is the most intense.

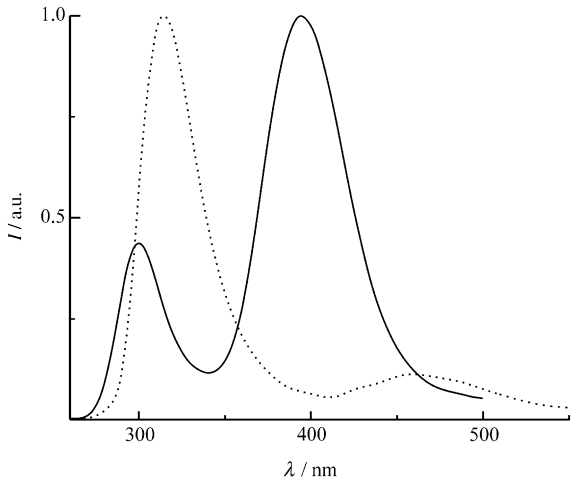

Figure 6. Luminescence spectra of fluorenone in cyclohexane (~10^{-5} M, dashed line) and in zeolite L ($p=0.2$, solid line), observed in air at 298 K. Fluorenone/zeolite L was excited at 250 nm, while fluorenone in cyclohexane was excited at 270 nm. The spectra are scaled to the same height at the maximum.

The results of temperature-dependent measurements made in the range of 293 K to 80 K with a fluorenone/zeolite L sample ($p=0.2$) are shown in Figure 7. In A) the sample was excited at 250 nm for each spectrum. The intensity of the band at 300 nm increases with decreasing temperature, whereas the opposite is true for the band at 400 nm; this is an unexpected observation. Graphs B) and C) show

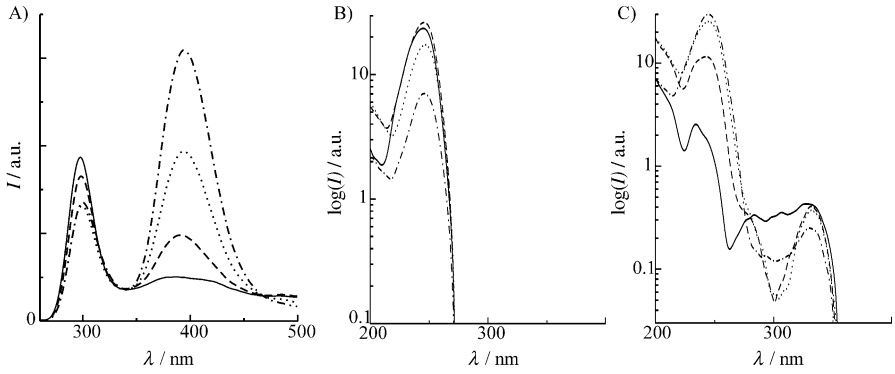

Figure 7. Luminescence and excitation spectra of fluorenone/zeolite L ($p=0.2$) at different temperatures: A) luminescence spectra, all excited at 250 nm, B) excitation spectra detected at 330 nm, and C) at 400 nm. The spectra were measured at the following temperatures (K): 80 (solid line), 150 (dashed line), 220 (dotted line), and 293 (dash-dot).

the temperature dependence of the electronic excitation spectra of each emission band. The excitation spectra detected at 330 nm (B) and 400 nm (C) have their maxima at the same wavelength and the band shape is similar, however, in C) a weak band at 370 nm is visible. Upon cooling, the intensities of the excitation spectra behave as expected from the luminescence spectra: the intensity increases for the spectra detected at 330 nm and decreases for the spectrum detected at 400 nm.

Time-resolved measurements: The luminescence lifetimes determined in this study are listed in Table 1. All measurements could be well fitted by assuming a single exponential decay. For fluorenone/zeolite L, the band at 400 nm has a surprisingly long lifetime of 115 μs, while that at 300 nm is about 9 μs. The lifetimes at the temperature of liquid nitrogen (77 K) are equal to those at room temperature, within the experimental error. In the case of fluorenone in solution, only the lifetime of the high-energy band could be determined as the intensity of the other band is too low. The lifetime of the band at 310 nm is the same in degassed and nondegassed solutions (both 11 μs). We have added data on singlet lifetimes and quantum yields from the literature for comparison.

Table 1. Luminescence lifetimes at room temperature for fluorenone in various solvents and for fluorenone/zeolite L.

λ [nm]	400	310	300	Ref.	Φ_F
fluorenone in solution:					
cyclohexane	–	11 μs[a]	–	1.8 ns[b]	–
methylcyclohexane	–	–	–	0.14 ns[c]	5.2×10^{-4}[c]
acetone	–	–	–	11.3 ns[b]	2.1×10^{-2}[c]
fluorenone/zeolite L:					
	115 μs[a]	–	9 μs[a]	–	–

[a] This work, excitation wavelength 240 nm. [b] Ref. [11], excitation wavelength 440 nm. [c] Ref. [12], excitation wavelength 360 nm.

Vibrational spectroscopy: Vibrational spectroscopy of molecule-loaded zeolites provides important information that can be used for qualitative and quantitative analytical purposes, as well as for investigating the influence of the zeolite on the inserted molecule. It was shown that for very thin zeolite layers coated on ZnSe wafers, quantitative information can be obtained by using the characteristic ν_{as}(T–O–T) or the δ(O–T–O) bands of the zeolite as an internal standard, in which T denotes either an Al^{3+} or an Si^{4+} ion.[20] If a similar procedure works for fluorenone/zeolite L, this could be used as a nondestructive analytical tool. We report the IR and Raman spectra, as well as the correlation of selected fluorenone IR and Raman band intensities with the dye loading. We then describe results of a normal coordinate analysis of fluorenone. The observed IR and Raman bands are collected in Table 3 with our calculated frequencies and experimental values from the literature.[21] The assignment of the fluorenone bands is based on our normal coordinate analysis and ref. [21], while the assignment of the zeolite L bands is based on refs. [20, 22–26].

IR spectra: We begin by comparing in Figure 8, the IR spectrum of fluorenone in a KBr pellet with the spectra of zeolite L and fluorenone/zeolite L coated as thin layers on a ZnSe plate and measured under high vacuum at room temperature between 500–3000 cm^{-1}. The spectra are plotted on a logarithmic scale because of the large difference in band intensity of the ν_{as}(T–O–T) zeolite band, with respect to the contributions of the fluorenone. The water bending vibration around 1645 cm^{-1}, usually seen as a strong feature in zeolite spectra, is hardly visible. This is due to the fact that thin zeolite L layers lose their water quickly under high vacuum, even at room temperature. Both spectra A) and B) display a very strong doublet around 1100 cm^{-1} and several weaker bands at 800 and 500 cm^{-1}, which all stem from the zeolite framework. Hence, the fluorenone/zeolite L spectrum is dominated by the very intense antisymmetric ν_{as}(T–O–T) stretching vibration at about 1050 cm^{-1}. However, the comparison of the thin-layer fluorenone/zeolite L spectrum with that of the fluorenone KBr pellet in the enlargement of the 1250–2000 cm^{-1} region illustrates that important bands belonging to the inserted fluorenone are well resolved, namely those at 1707, 1612, 1600, 1452, 1300, and 920 cm^{-1}. Data regarding the assignment will be given below. The major differences, with respect to the fluorenone KBr pellet spectrum, are a significant shift of the C=O stretching band from 1716 to 1707 cm^{-1}, the B_1 fundamental at 1523 cm^{-1} that appears only in the spectrum of the fluorenone/zeolite L sample, and a slight shift of the B_1 fundamental at 1452–1454 cm^{-1}.

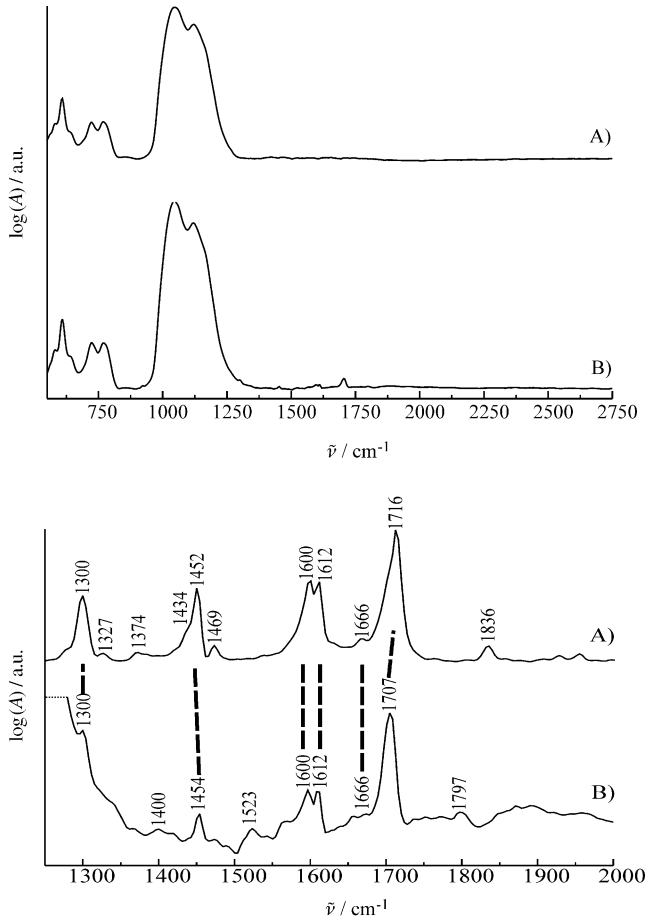

Figure 8. Top: IR absorption spectra of A) zeolite L and B) fluorenone/zeolite L ($p = 0.25$). Both recorded as thin layers on ZnSe plates. Bottom: Enlargement of the IR absorption spectra of A) fluorenone KBr pellet and B) fluorenone/zeolite L, in the region between 1250 and 2000 cm^{-1}. All spectra were recorded with a resolution of 8 cm^{-1} at a pressure of 2×10^{-5} mbar at room temperature.

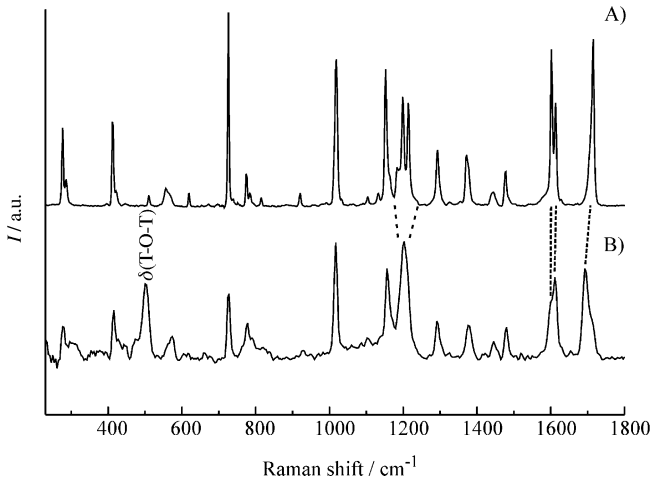

Figure 9. Raman spectra of A) crystalline fluorenone (200 scans) and B) a fully loaded fluorenone/zeolite L (4000 scans). Both spectra have a resolution of 8 cm^{-1}. Laser power on the sample was 300 mW, focused on approximately 0.12 mm^2.

Raman spectra: Figure 9 shows the Raman spectra of A) fluorenone and B) fluorenone/zeolite L. Both are rather weak Raman scatterers. The spectrum of the fluorenone/zeolite L system is less intense than that of a crystalline sample, so most of the weaker bands are not visible. This is accompanied by a broadening of the bands, and therefore some loss of structure; nevertheless, the main features are well resolved. The four-peak system of the crystalline sample, consisting of three fundamentals at 1214, 1198, and 1152 cm^{-1}, and of a combination band at 1183 cm^{-1}, is reduced to a group of two broad bands. The lowest peak shifts up to 1156 cm^{-1}, while the other three peaks form a single band with a maximum at 1200 cm^{-1}. The shift to lower energy of the C=O stretching band from 1714 to 1695 cm^{-1} is larger ($\Delta\tilde{\nu} = 20$ cm^{-1}) than in the IR spectrum. The position of all other fluorenone peaks remain unchanged. The peak at 500 cm^{-1} is due to the δ(T–O–T) of the zeolite.

Zeolite-framework vibrations as internal standard: An informative feature deriving from the vibrational spectra of a dye–zeolite L composite is the nondestructive, quantitative analysis of its dye content. Since the intensities (either the height or the integrated area of the peak) of the zeolite L band and the dye band are proportional to the amount of zeolite and dye, the zeolite L band acts as an internal standard and the ratio of the intensities leads to the dye concentration. The chosen peaks should be resolved and belong clearly to the zeolite or the dye. This method works for IR and Raman spectra.[20]

In this work the IR spectra were evaluated. The bands used for this correlation are indicated in Figure 10. The peak group from 563–841 cm^{-1}, stemming from the ν_s(T–O–T) of the zeolite, was used as the internal standard,

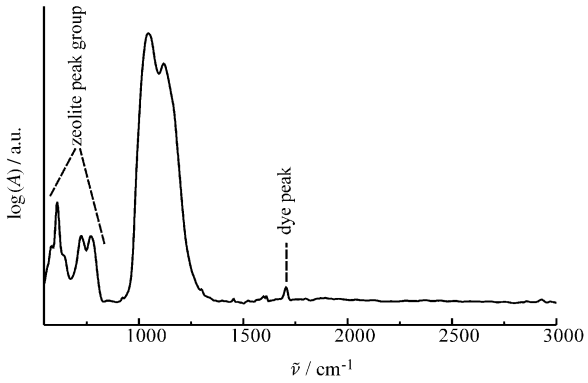

Figure 10. Bands used for the determination of the loading.

while the C=O stretching mode at 1707 cm^{-1} served as the dye peak. In Figure 11 a calibration curve is plotted: the horizontal axis shows the exact loadings of six fluorenone/zeolite L composites, as determined by dissolving the zeolite framework with HF (a conventional destructive method), and the vertical axis shows the ratios of the IR peaks. The dashed line shows the result obtained by using the ratio of the peak heights, while for the solid line the peak areas

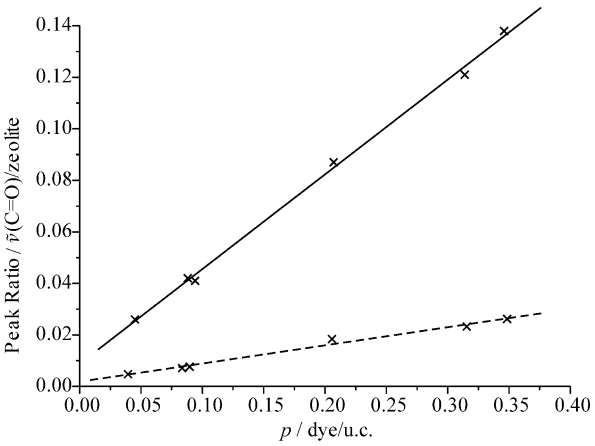

Figure 11. Correlation between the loading levels (dye molecules per u.c.) and dye–zeolite peak ratio. The ratio of the area of the dye to zeolite peaks is shown as solid line, while that of the heights is plotted as a dashed line.

were used. The correlation of the loading and the ratio of the fluorenone band to the zeolite-framework vibrations are linear in both cases.

Normal coordinate analysis: The use of symmetry coordinates improves the quality and reliability of the fitting procedure, in addition to simplifying the assignment of symmetry to the calculated frequencies. Once a correct assignment of the bands has been established and a good set of force constants has been found, internal coordinates are easier to use. The C_{2v} symmetry and the size of fluorenone make it natural to work with symmetry coordinates. Its 60 vibrational degrees of freedom are divided among the irreducible representations of the C_{2v} point group according to Equation (8):

$$\Gamma_{\mathrm{vib}} = 21\,\mathrm{A}_1 + 9\,\mathrm{A}_2 + 20\,\mathrm{B}_1 + 10\,\mathrm{B}_2 \qquad (8)$$

Out of the 66 symmetry coordinates given in Table 6 (see later), six are redundant (A_1:3; B_1:2; A_2:1). These redundant coordinates were not removed because most of the symmetrized force constants are the same as the internal force constants, due to the C_{2v} symmetry of the molecule (see Table 2). The remaining symmetrized force constants can be fully determined even if the six redundant coordinates remain; therefore their removal is not necessary. The eigenvalue problem factorizes accordingly, and the potential

Table 2. Force constants for fluorenone.

n[b]	Force const[a]	Value	n[b]	Force const[a]	Value	n[b]	Force const[a]	Value
				A				
1	F_R	10.484	6	$F_{R1R1'} = F_{R5R1''}$	1.383	30	$F^{p}_{R'\rho'} = F^{p}_{R''\rho''}$	0.089
	$F_{R1} = F_{R5}$	5.830	7	$F^{o}_{RR'} = F^{o}_{R''}$	1.562	32	$F^{m}_{\Omega'\rho'} = F^{m}_{\Omega''\rho''}$	−0.244
	$F_{R2} = F_{R4}$	6.796	9	$F^{m}_{RR'} = F^{m}_{RR''}$	0.464	33	$F^{o}_{\rho'\rho'} = F^{o}_{\rho''\rho''}$	−0.066
5	F_{R3}	4.758	11	$F^{p}_{RR'} = F^{p}_{RR''}$	0.249	34	$F_{\rho1'\rho3'} = F_{\rho1''\rho3''}$	0.215
8	$F_{R'} = F_{R''}$	7.814	10	$F^{o}_{R'R'} = F^{o}_{R''R''}$	1.822	35	$F_{\rho2'\rho4'} = F_{\rho2''\rho4''}$	0.069
14	$F_{r'} = F_{r''}$	4.973	12	$F^{m}_{R'R'} = F^{m}_{R''R''}$	0.150		$F_{\mu0\mu1'} = F_{\mu0\mu1''}$	0.055
17	$F_{\Omega1} = F_{\Omega4}$	2.230	13	$F^{o}_{R'r'} = F^{o}_{R''r''}$	−0.431	42	$F^{o}_{\mu'\mu'} = F^{o}_{\mu''\mu''}$	0.030
	$F_{\Omega2} = F_{\Omega3}$	1.907	15	$F_{R\Omega}$	1.437	44	$F^{m}_{\mu'\mu'} = F^{m}_{\mu''\mu''}$	0.001
23	$F_{\Omega'} = F_{\Omega''}$	2.426		$F_{R3\Omega2} = F_{R3\Omega3}$	1.302	45	$F^{p}_{\mu'\mu'} = F^{p}_{\mu''\mu''}$	0.044
31	$F_{\rho'} = F_{\rho''}$	0.789	16	$F_{R1'\Omega1} = F_{R1''\Omega4}$	−0.585		$F_{\mu4'\mu4''}$	−0.058
36	$F_{\rho0}$	2.552		$F_{R5'\Omega2} = F_{R5''\Omega3}$	−1.698		$F_{\mu0r2} = -F_{\mu0r1}$	1.933
58	$F_{\mu0}$	6.593	20	$F^{o}_{\Omega\Omega}$	−0.064		$F_{\mu0r4} = -F_{\mu0r5}$	0.047
43	$F_{\mu'} = F_{\mu''}$	0.188	27	$F_{\Omega2\Omega3}$	−0.916		$F_{\mu0r1'} = -F_{\mu0r1''}$	0.273
41	$F_{\mu1'} = F_{\mu1''}$	0.225	22	$F^{o}_{R'\Omega'} = F^{o}_{R''\Omega''}$	0.842	50	$F^{o}_{\mu'\tau'} = F^{o}_{\mu''\tau''}$	0.034
	$F_{\mu4'} = F_{\mu4''}$	0.151		$F^{o}_{R\Omega'} = F^{o}_{R\Omega''}$	0.842		$F_{\tau1r2}$	−0.391
	$F_{\tau1} = F_{\tau2}$	0.813	37	$F_{R1\Omega1'} = F_{R5\Omega1''}$	−0.855		$F_{\tau4r5}$	−0.522
	$F_{\tau4} = F_{\tau5}$	0.663	24	$F_{R3\Omega6'} = F_{R3\Omega6''}$	−0.612	48	$F_{\tau1r4} = F_{\tau2r5}$	0.206
57	$F_{\tau3}$	0.379		$F^{o}_{\Omega'\Omega'} = F^{o}_{\Omega''\Omega''}$	−0.034		$F_{\tau3r4} = F_{\tau3r5}$	0.046
53	$F_{\tau'} = F_{\tau''}$	0.570	25	$F^{m}_{\Omega'\Omega'} = F^{m}_{\Omega''\Omega''}$	−0.797	51	$F_{\tau1r1'} = F_{\tau2r1''}$	0.074
2	F^{o}_{R0}	2.378	26	$F^{p}_{\Omega'\Omega'} = F^{p}_{\Omega''\Omega''}$	−1.314	52	$F_{\tau4r'} = F_{\tau5r1''}$	0.645
	F_{R2R4}	−0.769	29	$F^{o}_{R'\rho'} = F^{o}_{R''\rho''}$	−0.151	54	$F_{\tau4r2'} = F_{\tau5r2''}$	0.183
	F_{R1R5}	2.177	28	$F^{m}_{R'\rho'} = F^{m}_{R''\rho''}$	0.096		$F_{\tau3r2'} = F_{\tau3r2''}$	0.096
				B				
3	$F_{R1} + F_{R1R5}$	8.007	40	$F_{\Omega2} - F_{\Omega2\Omega3}$	2.823	60	$F^{o}_{\mu'\mu'} - F_{\mu4'\mu4''}$	0.088
4	$F_{R2} + F_{R2R4}$	6.027	46	$F_{\mu'} + F_{\mu4'\mu4''}$	0.130	61	$2^{1/2} F_{\mu0r1}$	−2.734
18	$2^{1/2} F_{R3\Omega2}$	1.841	47	$F_{\tau1} + F_{\tau1r2}$	0.422	62	$F_{\tau1} - F_{\tau1r2}$	1.204
19	$0.5\,F^{o}_{R\Omega'}$	0.421	49	$F_{\tau4} + F_{\tau4r5}$	0.141	63	$2^{1/2} F_{\mu0r4}$	0.066
21	$F_{\Omega1} + F_{\Omega2\Omega3}$	1.314	55	$2^{1/2} F_{\tau3r4}$	0.065	64	$F_{\tau4} - F_{\tau4r5}$	1.185
38	$F_{R1} - F_{R1R5}$	3.653	56	$2^{1/2} F_{\tau3r2'}$	0.136	65	$2^{1/2} F_{\mu0r1'}$	0.386
39	$F_{R2} - F_{R2R4}$	7.565	59	$2^{1/2} F_{\mu0\mu1'}$	0.078			

[a] Force constants units: stretching constants [mdyn Å^{-1}]; bending constants [mdyn Å rad^{-2}]; stretch bend interactions [mdyn rad^{-1}]. Sub- and superscripts related to the symmetry coordinates (see Table 6 and Figure 19 later). [b] Internal force constants labeled with a number are used as symmetrized force constants without additional changes.

energy V_S for each symmetry species S consisting of SE elements can be expressed as shown in Equation (9):

$$V_S = \sum_{i=1,j=1}^{SE} F_{ij} S_i S_j \quad (9)$$

The symmetry force constants F^{SYM} given in Table 2 must be understood accordingly. Table 2 lists force constants for internal and symmetrized force fields. Constants labeled with a number correspond to symmetrized force constants. Part A of the table lists all internal force constants, as well as those that appear in the symmetrized force field without any changes (labeled by a number). Part B contains those symmetrized force constants which are different from the internal ones.

Force field: The starting point for generating the internal force field for fluorenone was to use a combination of the fields for cyclopentadiene and benzene. Additional force constants were introduced for the interaction between the central five-membered ring and both benzene rings. The internal force constants for cyclopentadiene[27] and benzene[28] were used as starting values, while those for the ring–ring interactions and for all constants involving the C=O bond were estimated. This trial force field, which contained more interactions than necessary, was fitted to the experimental IR and Raman frequencies.[21] After the first fitting we started to remove the superfluous interactions. The reduction procedure consisted of setting each off-diagonal term (or group of terms) in turn to zero. All force constants whose removal had no or only small influence on the frequencies were discarded. A new fit was performed after each reduction step. The A_2 modes were not included in the fit because they are IR inactive and only a few of them are present in the Raman spectra. The final force fields for each irreducible representation can be found in the Supporting Information. The resulting internal force constants are given in Table 2.

Frequencies: Table 3 lists the calculated frequencies, the experimental values from the literature,[21] and our measurements. The agreement between the calculated and observed values is quite good except for the lowest modes, for which the limits of the harmonic approach have probably been reached.

Influence of the zeolite host on the vibrational spectra: We now focus on identifying the modes which are most influenced by the zeolite host by using data from the spectra and normal coordinate analysis. In order to simplify the analysis, we have divided the spectra into regions containing similar modes. Some of these regions, especially in the lower frequency range, are overlapping.

Symmetrical and antisymmetrical C–H stretching vibrations (3100–3000 cm^{-1}): This region contains a system of four bands, each of them in fact being a combination of corresponding symmetrical and antisymmetrical C–H stretching vibrations. All eight modes show pure C–H stretching character. This system was actually not seen in the IR spectra of the fluorenone/zeolite L samples, probably due to its low intensity.

C=O stretching vibration (around 1720 cm^{-1}): The C=O stretching mode is one of the few bands that is strongly influenced by the zeolite host. In the case of the fluorenone/zeolite L system, the C=O stretching vibration is shifted to lower energy. Interestingly, the effect is more pronounced in the Raman spectrum (with $\Delta\tilde{\nu} = 20\ cm^{-1}$ instead of $\Delta\tilde{\nu} = 7\ cm^{-1}$). An additional shoulder also appears at 1705 cm^{-1}. The shift can be explained by assuming the coordination of the fluorenone's oxygen atom to an Al^{3+} site of the zeolite. Such coordination would result in a slight electron withdrawal and lowering of the bond order. This reduces the energy required for the bond stretching motion, which can be accurately simulated by lowering the force constant F_{Ro}.

6-Ring C–C stretching and C–H bending motion (1620–1130 cm^{-1}): These fundamentals exhibit a strong aromatic C–C stretching and a C–H bending character in the potential energy distribution. Two of these vibrations display a shift in the IR spectrum of the dye–zeolite system. The A_1 mode at 1597 cm^{-1} shifts to lower energy ($\Delta\tilde{\nu} = 3\ cm^{-1}$), while the B_1 at 1454 cm^{-1} moves up ($\Delta\tilde{\nu} = 4\ cm^{-1}$). It is interesting to note that the B_1 fundamental at 1523 cm^{-1} appears only in the spectrum of the fluorenone/zeolite L system. The other vibrations in this region show neither a change in position, nor any significant broadening. The situation in the Raman spectrum is quite different in that while there are little changes in the band positions, a broadening and change in the intensity ratio of the peaks at 1611 and 1603 cm^{-1} takes place. Also, the A_1 mode at 1152 cm^{-1} belongs to the quartet of peaks that is strongly influenced by the zeolite host: this band is broader and slightly shifted to a higher energy.

C–C stretching modes of the central ring (1440–1320 and 780–500 cm^{-1}): Many of these vibrations, although having a dominant 5-ring stretching character, display strong contributions from 6-ring deformations. It should be noted that the two B_1 modes at 1386 and 1322 cm^{-1} also exhibit strong C=O stretching and aromatic C–C bending character (both between 20% and 30%). Only the lower fundamental appears in our spectra and is unaffected by the zeolite. The bands in this region of the fluorenone/zeolite L spectra do not show any significant alterations when compared to the spectra of the free dye.

5- and 6-membered-ring stretching vibrations (1230–1100 cm^{-1}): The normal modes in this region have contributions from C–C bonds of all three rings and often display minor aromatic C–C bending character. Two A_1 modes in this region belong to a quartet of bands in the Raman spectrum that are influenced by the zeolite host. The two fully resolved sharp peaks in the crystalline fluorenone spectrum (1214 and 1192 cm^{-1}) merge into one broad band in the case of the dye–zeolite L sample. The broadening here is more pronounced than for the band system between 1611 and 1603 cm^{-1}.

Table 3. Experimental and calculated frequencies.

Symmetry type	Literature[a] IR	Literature[a] Raman	Observed[b] IR KBr	Observed[b] IR Zeolite L	Observed[b] Raman Crystalline	Observed[b] Raman Zeolite L	Calcd	Vibration type[c]
A_1	3082		3087				3085	$\tilde{\nu}(C-H)_{sym}$
B_1	3082		3087				3085	$\tilde{\nu}(C-H)_{asym}$
A_1	3072		3061				3068	$\tilde{\nu}(C-H)_{sym}$
B_1	3072		3061				3068	$\tilde{\nu}(C-H)_{asym}$
A_1	3049		3048				3046	$\tilde{\nu}(C-H)_{sym}$
B_1	3049		3048				3046	$\tilde{\nu}(C-H)_{asym}$
A_1	3026		3014				3032	$\tilde{\nu}(C-H)_{sym}$
B_1	3026		3014				3032	$\tilde{\nu}(C-H)_{asym}$
A_1	1728	1721	1716	1707	1714	1695	1727	$\tilde{\nu}(C=O)+\tilde{\nu}(C-C)$
B_1	1614	1615	1612	1610	1611	1611	1615	$\tilde{\nu}(C_{Ph}-C_{Ph})+\delta(C_{Ph}-H)$
A_1	1604	1606	1600	1600	1603	1603	1620	$\tilde{\nu}(C_{Ph}-C_{Ph})+\delta(C_{Ph}-H)$
A_1							1521	$\tilde{\nu}(C_{Ph}-C_{Ph})+\delta(C_{Ph}-H)$
B_1	1524						1533	$\tilde{\nu}(C_{Ph}-C_{Ph})+\delta(C_{Ph}-C_{Ph})+\delta(C_{Ph}-H)$
A_1		1481					1486	$\tilde{\nu}(C_{Ph}-C_{Ph})+\delta(C_{Ph}-H)$
B_1	1475		1473		1476	1479	1504	$\tilde{\nu}(C_{Ph}-C_{Ph})+\delta(C_{Ph}-C_{Ph})+\delta(C_{Ph}-H)$
B_1	1455		1452	1454			1447	$\tilde{\nu}(C_{Ph}-C_{Ph})+\delta(C_{Ph}-H)$
A_1	1436	1447			1442	1445	1431	$\tilde{\nu}(C-C)+\delta(C_{Ph}-H)$
B_1	1394						1386	$\tilde{\nu}(C-C)+\delta(C=O)+\delta(C_{Ph}-C_{Ph})$
A_1	1375	1375	1374		1372	1372	1387	$\tilde{\nu}(C_{Ph}-C_{Ph})+\delta(C_{Ph}-H)$
B_1	1325		1326		1329		1322	$\tilde{\nu}(C-C)+\delta(C=O)+\delta(C_{Ph}-C_{Ph})+\delta(C-C)$
B_1	1300		1300	1300			1298	$\delta(C_{Ph}-H)+\tilde{\nu}(C_{Ph}-C_{Ph})+\tilde{\nu}(C-C)$
A_1		1239			1293	1292	1321	$\delta(C_{Ph}-C_{Ph})+\tilde{\nu}(C-C)$
B_1	1237		1234				1225	$\tilde{\nu}(C_{Ph}-C_{Ph})+\delta(C_{Ph}-C_{Ph})+\tilde{\nu}(C-C)$
A_1		1214			1214		1240	$\tilde{\nu}(C_{Ph}-C_{Ph})+\tilde{\nu}(C-C)+\delta(C_{Ph}-C_{Ph})$
A_1		1198			1198		1179	$\tilde{\nu}(C_{Ph}-C_{Ph})+\tilde{\nu}(C-C)+\delta(C_{Ph}-H)$
B_1	1192		1192				1164	$\tilde{\nu}(C_{Ph}-C_{Ph})+\tilde{\nu}(C-C)+\delta(C_{Ph}-H)+\delta(C_{Ph}-C_{Ph})$
A_1	1152	1155	1151		1152	1155	1132	$\tilde{\nu}(C_{Ph}-C_{Ph})+\delta(C_{Ph}-H)$
				1119				$\tilde{\nu}_{as}(T-O-T)$[d]
B_1	1100	1100	1098		1102		1100	$\tilde{\nu}(C_{Ph}-C_{Ph})+\tilde{\nu}(C-C)+\delta(C_{Ph}-H)+\delta(C_{Ph}-C_{Ph})$
				1045				$\tilde{\nu}_{as}(T-O-T)$[d]
A_2							1041	$\tau(H-C_{Ph}-C_{Ph}-H)+\gamma(C_{Ph}-H)$
A_1	1018	1019	1011		1017	1018	1023	$\delta(C_{Ph}-H)+\tilde{\nu}(C_{Ph}-C_{Ph})$
B_1	1008						1003	$\delta(C_{Ph}-H)+\tilde{\nu}(C_{Ph}-C_{Ph})$
A_2							953	$\tau(H-C_{Ph}-C_{Ph}-H)+\gamma(C_{Ph}-H)+\tau(C-C-C-C)$
B_2	952		954				981	$\tau(H-C_{Ph}-C_{Ph}-H)+\gamma(C_{Ph}-H)$
A_1							927	$\delta(C_{Ph}-H)$
B_1	919	921	921	921	921	927	895	$\delta(C_{Ph}-H)+\tilde{\nu}(C_{Ph}-C_{Ph})$
B_2	880		885				903	$\gamma(C_{Ph}-H)+\tau(C-C-C-C)+\gamma(C=O)$
B_2	812		813		816		817	$\gamma(C=O)+\tau(C-C-C-C)+\gamma(C_{Ph}-H)$
A_2							786	$\gamma(C_{Ph}-H)+\tau(H-C_{Ph}-C_{Ph}-H)$
A_1	774	776			775	776	778	$\tilde{\nu}(C-C)+\tilde{\nu}(C=O)+\delta(C_{Ph}-C_{Ph})$
				769				$\tilde{\nu}_s(O-T-O)$[d]
B_2	741		738				727	$\tau(C-C-C-C)+\gamma(C=O)$
A_1	723	726			725	727	706	$\delta(C_{Ph}-C_{Ph})+\tilde{\nu}(C-C)$
				723				$\tilde{\nu}(AlO_4)$[d]
B_2	672		671				663	$\gamma(C=O)+\tau(C-C-C-C)+\gamma(C_{Ph}-H)$
B_1	652		650				681	$\delta(C_{Ph}-C_{Ph})+\tilde{\nu}(C-C)$
A_2							667	$\gamma(C_{Ph}-H)+\tau(H-C_{Ph}-C_{Ph}-H)$
B_1	619		617				587	$\delta(C-C)+\tilde{\nu}(C_{Ph}-C_{Ph})+\tilde{\nu}(C-C)+\delta(C_{Ph}-C_{Ph})$
				608				$\tilde{\nu}(D6)$[d]

Table 3. (Continued)

Symmetry type	Literature[a] IR	Literature[a] Raman	Observed[b] IR KBr	Observed[b] IR Zeolite L	Observed[b] Raman Crystalline	Observed[b] Raman Zeolite L	Calcd	Vibration type[c]
				582				unassigned[d]
A_1	566	566	561		558		533	$\delta(C_{Ph}-C_{Ph})+\tilde{\nu}(C_{Ph}-C_{Ph})+\tilde{\nu}(C-C)$
B_2	551						576	$\tau(C-C-C-C)+\gamma(C_{Ph}-H)+\gamma(C=O)$
A_2							513	$\gamma(C_{Ph}-H)$
B_1	501	509	509		510		504	$\tilde{\nu}(C-C)+\delta(C_{Ph}-C_{Ph})+\tilde{\nu}(C_{Ph}-C_{Ph})$
						500		$\delta(O-T-O)$[d]
A_2							487	$\gamma(C_{Ph}-H)+\tau(H-C_{Ph}-C_{Ph}-H)$
B_2	436						404	$\gamma(C_{Ph}-H)+\gamma(C=O)+\tau(H-C_{Ph}-C_{Ph}-H)$
A_2							343	$\tau(C-C-C=O)+\gamma(C_{Ph}-H)$
A_1	403	411			412	413	425	$\delta(C-C)+\delta(C_{Ph}-C_{Ph})+\tilde{\nu}(C-C)$
B_2	392						363	$\tau(H-C_{Ph}-C_{Ph}-H)+\gamma(C_{Ph}-H)$
B_1	278	282			276	277	259	$\tilde{\nu}(C-C)+\delta(C_{Ph}-C_{Ph})+\tilde{\nu}(C_{Ph}-C_{Ph})$
A_2		273					222	$\gamma(C_{Ph}-H)+\tau(H-C_{Ph}-C_{Ph}-H)$
A_1	204	207			210		196	$\delta(C-C)+\delta(C_{Ph}-C_{Ph})+\tilde{\nu}(C-C)$
B_2	159	160			167		164	$\tau(C-C-C-C)+\gamma(C=O)$
A_2							27	$\tau(H-C_{Ph}-C_{Ph}-H)+\tau(C-C-C-C)+\gamma(C_{Ph}-H)$
B_2	120						19	$\tau(C-C-C-C)+\gamma(C=O)+\tau(H-C_{Ph}-C_{Ph}-H)$

[a] Taken form ref. [21], all frequencies given in cm^{-1}. [b] All frequencies given in cm^{-1}. [c] Types of vibration: $\tilde{\nu}$ = stretch, δ = bending, γ = out-of-plane motion, τ = torsion. [d] Zeolite bands, see refs. [20, 22–26]

C–H bending motions (1030–890 cm^{-1}): Three of the four C–H bending modes in this region also display an aromatic C–C stretching character. Only two of them are present in either the IR or the Raman spectra. They do not show any sign of being influenced by the zeolite host.

6-Ring deformation modes (710–530 cm^{-1}): These bending modes exhibit an additional 5-ring stretching character. Only the A_1 fundamental at 562 cm^{-1} is influenced by the host. It is shifted to higher energy in the Raman spectrum of fluorenone/zeolite L ($\Delta\tilde{\nu}=8$ cm^{-1}).

5-Ring deformation modes (590–190 cm^{-1}): The 5-ring deformation modes also show 5-ring stretching and 6-ring bending character. They do not seem to be very influenced by the zeolite host.

Torsional and out-of-plane vibrations (400–19 cm^{-1}): Most of the higher energy modes of this type have A_2 symmetry and are therefore inactive. The few modes present in the Raman spectra are not influenced by the host.

Molecular orbital calculations: Molecular orbital calculations have been performed in order to understand the electronic structure of the guest, host, and the host–guest system. We first consider the one-electron orbitals of fluorenone and study the influence of configuration interaction (CI) on the π-electron states. Then we investigate the influence of the zeolite host on the electronic structure of the guest.

One-electron orbitals: The frontier-orbital region of fluorenone, as obtained by an extended-Hückel molecular orbital (EHMO) calculation, is depicted in Figure 12. The HOMO is an n orbital of b_1 symmetry and the LUMO is a π orbital of b_2 symmetry. The largest contribution to the HOMO stems from the carbonyl-oxygen atom and the remaining part is concentrated on the "upper" half of the molecule. The π and π* orbitals in the frontier-orbital region are of either a_2 or b_2 symmetry. The former have a node at the carbonyl group for symmetry reasons. The $1\pi(a_2)$ orbital, which lies well below the $1n(b_1)$, is spread out over both phenyl rings, while the LUMO $1\pi^*(b_2)$ is more concentrated on the central ring and has a large contribution from the carbonyl group. From this we conclude that the most important frontier-orbital interactions of the carbonyl group with the zeolite framework are to be expected with the LUMO, HOMO, and HOMO−2 levels. All electronic n–π* transitions are symmetry forbidden, as the π orbitals are of either a_2 or b_2 symmetry. Only *x* or *z* polarized transitions will have non-zero oscillator strengths. Calculated oscillator strengths and the square of transition-dipole lengths for relevant transitions are given in Table 4. As expected, the square of the transition-dipole lengths of all n–π* transitions is zero and is small for the first π–π* transition ($1\pi^*\leftarrow1\pi$). The oscillator strength of the latter is about 30 times smaller than that of

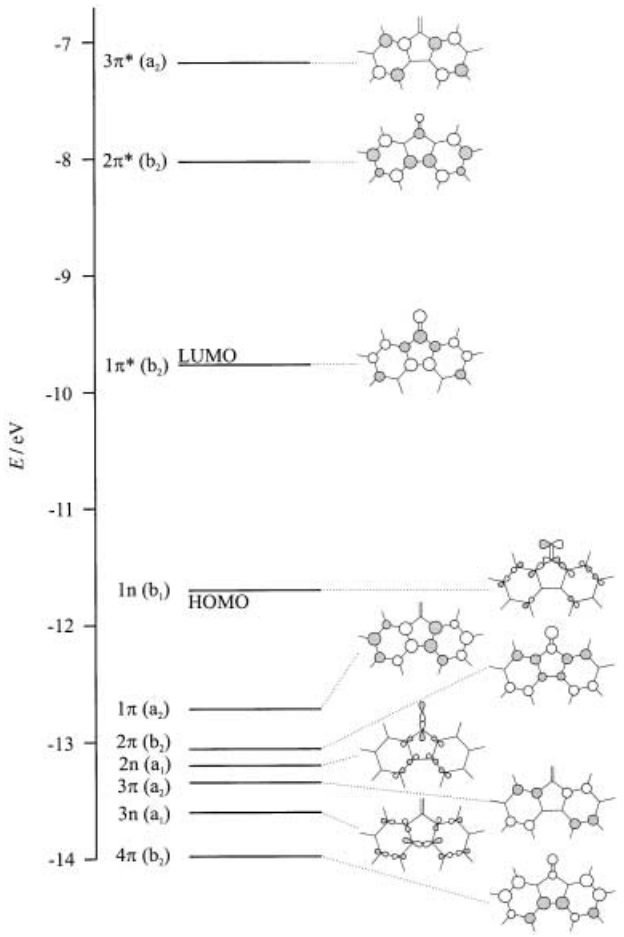

Figure 12. One-electron energy level diagram of fluorenone and MO diagrams.

Table 4. Calculated oscillator strengths f and the square of transition-dipole lengths $|D_{nm}|^2$. A dash (–) replaces the values for symmetry forbidden transitions.

Transition	Symmetry	Polarization	$\lvert D_{nm}\rvert^2$ [Å^2]	$f(xyz)$
1π*←1n	A_2	–	–	–
1π*←1π	B_1	x	0.243	0.030
1π*←2π	A_1	z	0.983	0.556
1π*←2n	A_2	–	–	–
1π*←3π	B_1	x	0.846	0.449
1π*←3n	A_2	–	–	–
2π*←1n	A_2	–	–	–
2π*←1π	B_1	x	1.101	0.993
2π*←2π	A_1	z	0.412	0.149
2π*←2n	A_2	–	–	–
2π*←3π	B_1	x	0.266	0.066
2π*←3n	A_2	–	–	–

the 2π*←1π transition which has the largest value (0.993). The 1π*←2π and 1π*←3π transitions also display large oscillator strengths.

Configuration interaction: Mixing of the HOMO 1n(b_1) with σ orbitals of the same symmetry is negligible, mainly because they are too far away in energy. Hence, it is sufficient to study the influence of CI on the π levels, which was carried out by using the Pariser–Parr–Pople (PPP) procedure. The result of a CI treatment with 49 configurations is shown in Figure 13. The electronic configurations given in this figure are identified only by the two highest occupied orbitals, so the ground-state configuration $(2n)^2(2\pi)^2(1\pi)^2(1n)^2$ is abbreviated to $(1n)^2$. We observe that the $S_{1\pi}$ state is shifted to higher energy, but can still be mainly attributed to the 1π*←1π transition. However, the energy splitting between the $S_{1\pi}$ and $S_{2\pi}$ states is large (about 0.8 eV). The $S_{2\pi}$ and $S_{3\pi}$ states come very close, but the successions of symmetries remain unchanged in the region of interest. The gap between the $S_{3\pi}$ and the $S_{4\pi}$ states is about as large as the gap observed between the $S_{1\pi}$ and $S_{2\pi}$ states. The $S_{2\pi}$ and $S_{3\pi}$ states display significant contributions from high-energy configurations, such as $(2\pi^*)^1(2\pi)^1$ and $(3\pi^*)^1(1\pi)^1$ for $S_{2\pi}$, or $(2\pi^*)^1(1\pi)^1$ for $S_{3\pi}$. The higher lying $S_{4\pi}$ and $S_{5\pi}$ states show contributions from low-energy configurations, like $(1\pi^*)^1(2\pi)^1$ or $(1\pi^*)^1(3\pi)^1$ for $S_{4\pi}$ and $S_{5\pi}$, respectively. The six π–π* transitions obtained at 389, 314, 312, 257, 249, and 231 nm are in good agreement with the measured electronic absorption spectrum shown in Figure 5. Calculated oscillator strengths and the polarization for relevant transitions are given in Table 5. Charge is redistributed upon electronic transition. We illustrate this in Scheme 1 for the S_0 and $S_{1\pi}$ states. The main observation is that charge is transferred to the carbonyl group upon $S_{1\pi}$←S_0 electronic excitation, with the oxygen atom displaying the largest increase (from 1.19 to 1.48).

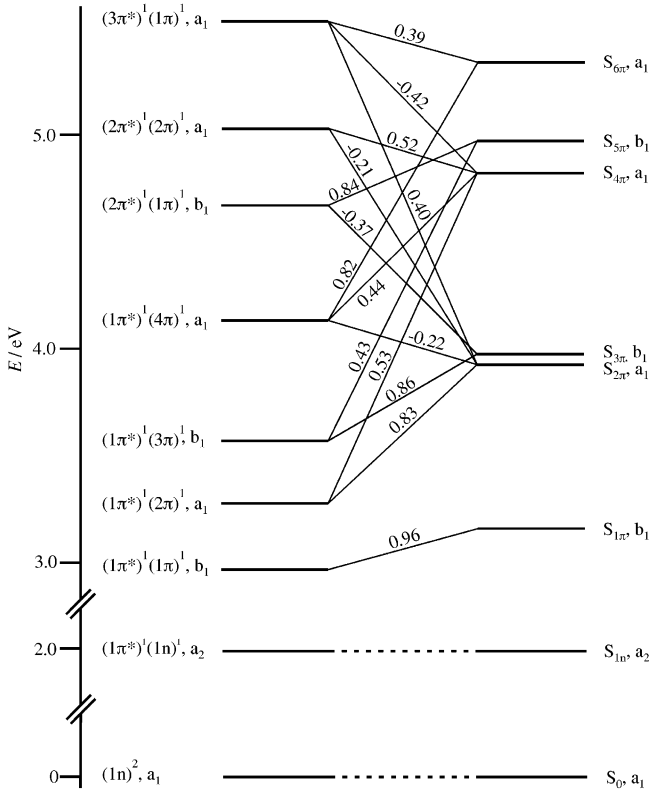

Figure 13. Correlation of the electronic configuration of fluorenone (left) and the electronic states after CI (right). The contribution of an electronic configuration to a state is indicated by the number above the connecting line.

Table 5. Calculated oscillator strengths.

Transition	ΔE [cm^{-1}]	Wavelength [nm^{-1}]	Polarization	f
$S_{1\pi} \leftarrow S_0$	25697	389	x	0.066
$S_{2\pi} \leftarrow S_0$	31813	314	z	0.204
$S_{3\pi} \leftarrow S_0$	31999	312	x	0.052
$S_{4\pi} \leftarrow S_0$	38910	257	z	0.488
$S_{5\pi} \leftarrow S_0$	40160	249	x	1.107
$S_{6\pi} \leftarrow S_0$	43290	231	z	0.002

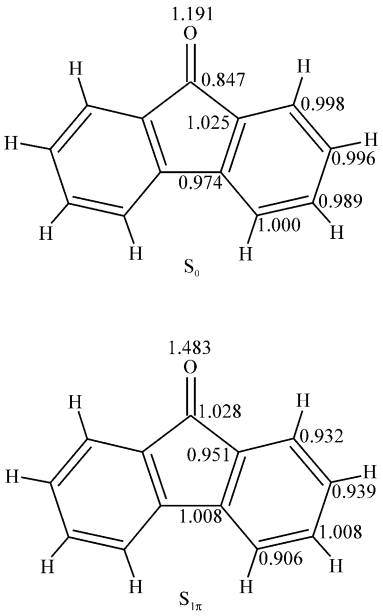

Scheme 1. Charge distribution for the S_0 and $S_{1\pi}$ states.

Influence of the zeolite host on the electronic structure of the guest: Based on our experimental findings and on chemical reasoning, we expect that the main influence of the zeolite on the frontier orbitals of fluorenone can be expected from interaction of the carbonyl group with the Al^{3+} and Si^{4+} sites of the zeolite. A way to model such an interaction is to study the behavior of the fluorenone orbitals in a molecular approach, as a function of the distance between the Al^{3+} ion and O atom, in the arrangement illustrated in Scheme 2.

Scheme 2. Geometrical arrangement used for modeling the interaction between fluorenone and $Al(OH)_4^-$. The distance d is measured from the center of the oxygen atom to the center of the aluminium atom. Oxygen is shown in dark grey, hydrogen in white, carbon in light gray, and aluminum in black.

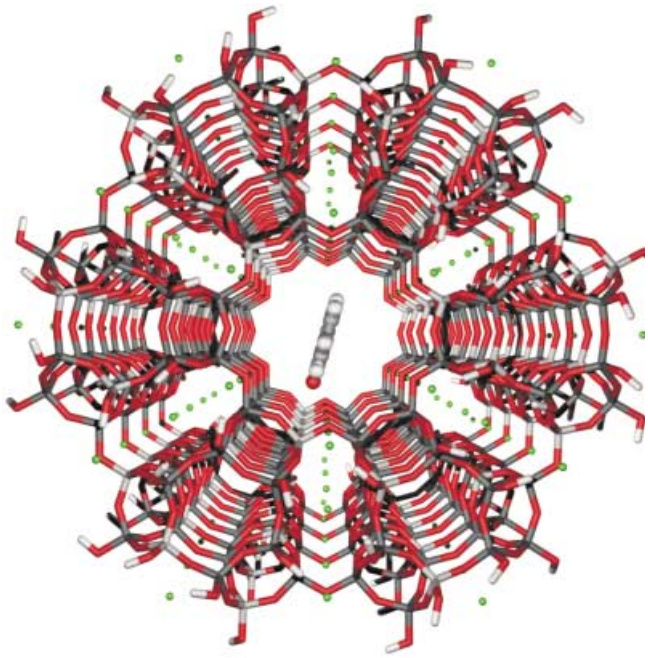

Figure 14. Orientation of a fluorenone molecule in a channel of zeolite L as used in the calculation. Fluorenone is oriented so that its oxygen atom points towards a zeolite Al^{3+} site, with an $Al^{3+}\cdots O$ distance of 0.24 nm. Oxygen is shown in red, hydrogen in white, aluminum in light gray, and silicon in dark gray. Green spheres represent counterions (Na^+ and K^+). The whole system consists of 1606 atoms.

A more involved way is to place the fluorenone at different positions in the zeolite L channel as illustrated in Figure 14.

In the molecular approach, a fluorenone molecule was placed at a large distance from an $Al(OH)_4^-$ ion (9.9 nm). The molecule was oriented in such a way that the carboxyl group is pointing towards the aluminum ion with a minimum of symmetry reduction, as shown in Scheme 2. Distances are measured from the center of the oxygen atom to the center of the aluminum ion. The distance between the molecule and the ion was then gradually reduced and the effect on the energy levels and MO was monitored. Results of this simulation for the relevant frontier orbitals are depicted in Figure 15. Up to a distance of 0.5 nm, the MOs and energy levels remain unperturbed. At a distance of less than 0.23 nm, the model of a separate molecule and ion breaks down and severe mixing of MOs occurs. The energy of the 2π orbital increases strongly with decreasing distance, but always remains below the 1π MO. As expected, the 1π orbital is not affected by the presence of the aluminum cation. The 1n and $1\pi^*$ levels move to higher energy with decreasing $Al^{3+}\cdots O$ distance. The 1π–$1\pi^*$ gap increases when a fluorenone molecule approaches an Al^{3+} ion, which corresponds to a hypsochromic shift of the transition. We note that this correlates well with the observed behavior.

Another way of studying the carbonyl–zeolite interaction is to place a fluorenone molecule inside a zeolite L channel. The channel section chosen is large enough so that border effects can be neglected. The system, consisting of the channel section and a dye, contains 1606 atoms. The fluorenone molecule was oriented so that the oxygen atom is directed towards an aluminum ion in the channel wall. The $Al^{3+}\cdots O$

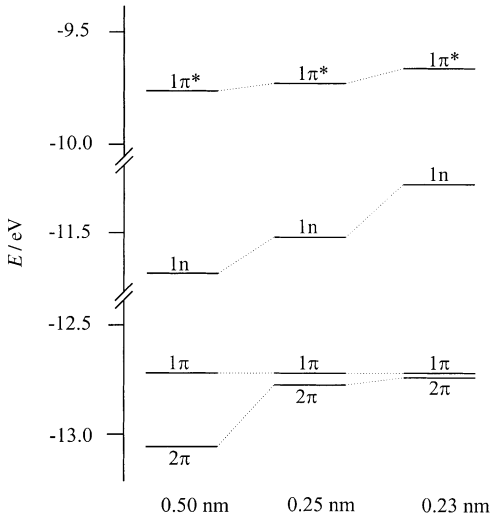

Figure 15. Correlation diagram of the energy of frontier orbitals of fluorenone as a function of decreasing Al^{3+}···O distance.

distance was set to 0.25 nm. Care was taken to insure that the fluorenone's oxygen atom was at least 0.18 nm away from the closest oxygen atoms of the zeolite. The distance between the hydrogen atoms and the walls was always larger than 1.00 nm. This arrangement is illustrated in Figure 14. It should be stressed that this is only one of many possible meaningful orientations. This orientation was chosen according to simple theoretical reasoning. The main interaction is expected to occur between the oxygen atom of the carboxyl group and an Al^{3+} site. The distance of the remaining atoms of fluorenone to the channel walls should be kept large in order to minimize their interactions. The density of levels (DOL) and the local density of levels (L-DOL) are very useful in order to investigate the effects of the host on the fluorenone molecule. For an explanation of the concept of DOL and L-DOL, we refer to refs. [29–31]. Figure 16 displays the calculated DOL of a) fluorenone and c) zeolite L , as well as b) the L-DOL of fluorenone/zeolite L. An important feature is that the HOMO of zeolite L

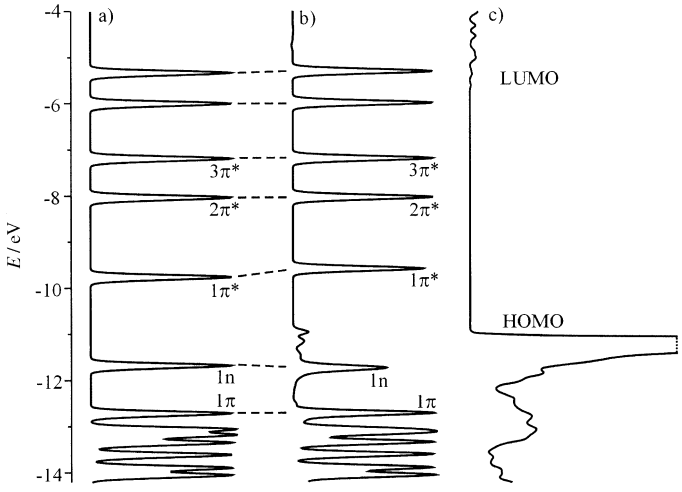

Figure 16. Calculated DOL of a) fluorenone and c) zeolite L, and b) the L-DOL of fluorenone in zeolite L. Curves a) and b) have been magnified by a factor of 100.

lies at a higher energy than the HOMO of fluorenone. The simulation also shows that the 1π, 2π*, and 3π* orbitals are not influenced by the presence of the zeolite host, whereas the 1π* shifts to higher energy. The 1n level is pushed to a slightly lower energy by the interaction with the host. Some additional fluorenone L-DOL appear in the case of b) in the HOMO–LUMO gap. This is due to some slight mixing of oxygen orbitals of fluorenone with the orbitals of zeolite L. This more complex model also shows that the 1π–1π* gap increases when the fluorenone's oxygen atom approaches an Al^{3+} site, which corresponds well with the observed hypsochromic shift of the lowest emission.

Discussion

The properties of fluorenone/zeolite L were investigated experimentally by means of electronic absorption, luminescence, IR, and Raman spectroscopy, TGA, and DSC. The experimental results show evidence of interactions between fluorenone and the zeolite host. The MO calculations and normal coordinate analysis allowed us to understand and model these observations. The combined experimental and theoretical results give quite a clear picture of the host–guest interactions that will be described in this section.

Influence of coadsorbed water on the dye location: The washing of dry dye–zeolite L material with 1-butanol, which was first studied for resorufin/zeolite L,[32] allows the distinction to be made between dyes located inside and outside of the channels. It is also used to remove molecules from the surface of the crystals, which is necessary for all spectroscopic measurements. The washing procedure can only remove dye molecules adsorbed onto the outer surface of the zeolite crystals. The steric conditions of fluorenone located in a channel prevent large solvent molecules like 1-butanol from passing the dye. This implies that the solvation of fluorenone located inside the channels is not possible, and hence cannot be removed. The washing experiments showed that there is no difference between the amount of fluorenone located on the surface of dry and rehydrated material. In addition, the quantity of fluorenone found after dissolving the zeolite framework was identical for both materials. This proves that coadsorbed water does not displace fluorenone from the channels of zeolite L.

Thermal analysis: Two important differences can be observed between the TGA of fluorenone/zeolite L composites and those of its components alone. Firstly, the desorption maximum of water appears at a lower temperature in the fluorenone/zeolite L system (100 °C instead of 110 °C). Secondly, the loss of dye in this material happens in two steps at much higher temperatures (at 500 °C and 680 °C instead of 270 °C). This shift to higher temperature points to a significant interaction between the dye and the zeolite framework. The lower desorption temperature of water can be regarded as fluorenone acting like an impurity. Another possible explanation is that fluorenone molecules occupy the positions that water would otherwise be bound to. Because

fluorenone is not displaced by water from these positions, some water molecules will be less strongly bound to the zeolite channel. This in turn results in a lower desorption temperature. The DSC analysis shows that the zeolite phase transition occurs at lower temperature in the case of the fluorenone/zeolite L material. This behavior could also be explained by looking at fluorenone acting as an impurity from the point of view of the zeolite.

Electronic spectroscopy and molecular orbital calculations: The results obtained from electronic spectroscopy and MO calculations are summarized in Figure 17. The left side shows the calculated energy levels and the oscillator

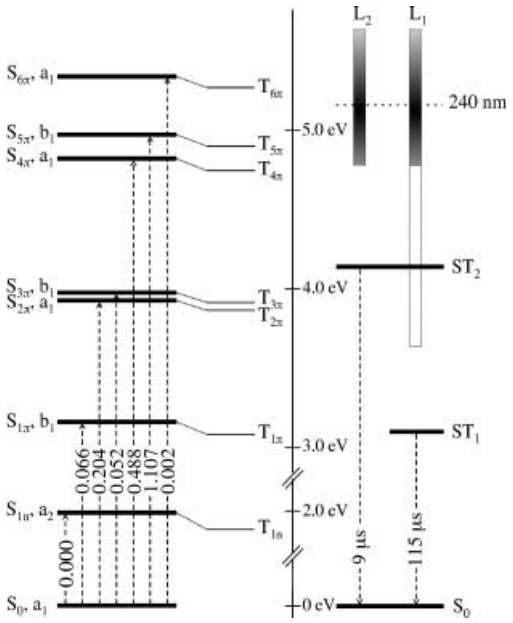

Figure 17. Energy states diagram for fluorenone/zeolite L. Left side: calculated energy levels (with CI) and oscillator strengths. Right side: observed luminescence (ST_1, ST_2), excitations (L_1, L_2), and lifetimes. Excitation spectra are depicted as boxes and the shading corresponds to the spectral intensity. Darker shading represents a stronger signal.

strengths. According to the oscillator strengths, fluorenone can be excited from the S_0 state to the $S_{1\pi}$, $S_{2\pi}$, $S_{3\pi}$, $S_{4\pi}$, and $S_{5\pi}$ states, but not to the lowest lying state (1n). The right side of Figure 17 summarizes data obtained from the luminescence spectra of fluorenone/zeolite L. The two observed luminescence maxima are labeled as ST_1 and ST_2. Excitation spectra are depicted as boxes (L_1 and L_2) with the shading proportional to the spectral intensity, darker shadings stand for stronger signals. Using light with a wavelength of 240 nm, the molecule can be excited to the $S_{5\pi}$ or $S_{4\pi}$ state. It is interesting that the molecule shows two distinct luminescence bands instead of just relaxing radiationlessly into the lowest state and emitting light from there. From the calculation, the ST_1 state could correspond to either $S_{1\pi}$ or $T_{1\pi}$, while the ST_2 state could be attributed to $S_{2\pi}$ or $T_{2\pi}$. We name these states ST_1 and ST_2 because their spin state has not been proven. The long lifetime would be consistent with an assignment as $T_{1\pi}$ and $T_{2\pi}$, respectively. The temperature-dependent spectra show that ST_1 is populated by means of a thermally activated process. It should also be noted that the ST_1 band is much weaker in solution. The interaction with the zeolite host seems to favor the populating process of the ST_1 state. The luminescence spectra show no band that could be attributed to the $S_{1n} \leftarrow S_0$ transition. We can conclude that the zeolite–fluorenone interaction does not lead to a sufficient symmetry reduction that would make the $S_{1n} \leftarrow S_0$ transition allowed.

Influence of the zeolite host on the electronic structure of the guest: One point that has to be considered is the significant hypsochromic shift of the luminescence and the excitation bands for the fluorenone/zeolite L composite. The MO diagrams give some clues to the nature of the interactions between fluorenone and the zeolite host and its influence on the electronic spectra. Transitions from the 1π to the $1\pi^*$ orbitals involve a shifting of the π-electron density from the phenyl rings to the carbonyl group. This is the reason for the blueshift of the $S_{1\pi} \leftarrow S_0$ emission band. The shift of the second band is more difficult to explain, because substantial CI takes place. An interaction of the fluorenone's oxygen atom with a framework Al^{3+} ion or counterion would have little-to-no effect on the 1π energy level, as this MO has no contributions from the carbonyl group. The $1\pi^*$ and 2π MOs, however, would be destabilized in such a situation. The simulations we performed tended to confirm this. The 1π–$1\pi^*$ gap increases when a fluorenone molecule approaches an Al^{3+} ion, which corresponds to a hypsochromic shift of the transition. The models of fluorenone interacting with $Al(OH)_4^-$ and of the dye located inside a channel section succeeded in a qualitative reproduction of the observed trend in the luminescence spectra of fluorenone/zeolite L.

Zeolite-framework vibrations as internal standard: The quantitative determination of the dye loading by evaluation of the vibrational spectra has been successfully applied to the fluorenone/zeolite L system. The zeolite-framework vibrations can be used as internal standards and provide us with a fast, nondestructive method of measuring the dye content of such samples. Taking the weaker zeolite bands as internal standard instead of the intense ν_{as}(T–O–T) vibrations makes it possible to work with thicker layers. The benefit of using thick layers is an increase in sensitivity to dye vibrations, without having a saturated internal standard. This modification to the method allows the accurate determination of loadings of even less than 0.05 dye molecules per unit cell, which is quite an improvement compared with results reported earlier.[20] The results obtained in this study are proof that this method can also be extended to other dye–zeolite material.

IR and Raman spectra: Comparing the spectra shows that the zeolite bands are not influenced by the inserted dye molecules. The spectra lead to the conclusion that the structure of fluorenone is left nearly unchanged upon insertion into zeolite L. The most important change occurs in the C=O bond, which gets weakened by the interaction of the oxygen with an Al^{3+} site of the zeolite. Aluminum sites with

coordination numbers higher than four have been recently reported in Mordenite and zeolite Beta at room temperature.[33] Other modes that are influenced by the zeolite host are motions that display mainly aromatic ring bending and 5- and 6-ring stretching character. These modes are shifted to higher energy. This suggests that the molecule sits close enough to the channel walls so that the aromatic 6-rings can interact with the zeolite's counterions (K^+). Experimental results and calculations have shown that the preferred adsorption sites for benzene in zeolite L are the counterions located in the channel walls.[34–37] Such a position would result in a slight hindrance of these motions and an increase of the energy needed to activate them. These observations led to the model shown in Scheme 3.

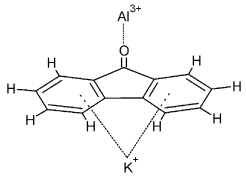

Scheme 3. Model of the interactions between fluorenone and zeolite L. Most of the observed changes in electronic spectra can be attributed to the strong $Al^{3+}\cdots O$ interaction. The interaction of the aromatic rings with a zeolite counterion (K^+) is visible in the vibrational spectra only.

Conclusion

We conclude that the fluorenone/zeolite L material is now so well understood that it would make an excellent system for applying advanced force field and quantum chemical calculations. With the help of MO calculations, the presence of two luminescence bands can be understood. The changes in electronic spectra and in desorption temperature can be attributed mainly to the $Al^{3+}\cdots O$ host–guest interaction. This interaction, as well as that of the aromatic 6-rings with a counterion of zeolite L (K^+), can be seen in the vibrational spectra. Through these investigations, a better comprehension of the unconventional behavior of fluorenone has been achieved.

Experimental Section

Materials: The pure potassium form of zeolite L ($K_9(AlO_2)_9(SiO_2)_{27}\cdot 21H_2O$) was synthesized as described in ref. [38]. The morphology of the zeolite L crystals is shown in Figure 1. The average length of the crystals used in this study was about 600 nm. Fluorenone (Fluka, 99%) was used as received. 1-Butanol (Aldrich, for UV spectroscopy, >99.5%) and cyclohexane (Merck Uvasol, 99.9%) were used as solvents without further purification. The extinction coefficients of fluorenone in 1-butanol and cyclohexane were determined as $\varepsilon_{(257\,nm)}=9.0\times10^4$ and $\varepsilon_{(256\,nm)}=1.0\times10^5\,L\,mol^{-1}\,cm^{-1}$, respectively. Fluorenone sublimates at 100 °C at a pressure of 0.7 mbar.

Synthesis of fluorenone/zeolite L composites: Fluorenone can be inserted into the channels of zeolite L through the solid-gas equilibrium shown in Equation (10):

$$ZD_{r-1} + D(g) \rightleftharpoons ZD_r \quad (10)$$

in which $D(g)$ denotes the dye molecules in the gas phase and ZD_r those in the channels of the zeolite. The parameter r is the number of sites occupied by dye molecules. Its value ranges from 0 to n_s, for which n_s is equal to the number of sites in one channel. Fluorenone/zeolite L can be prepared by using the double-ampoule method.[2] The zeolite was first dried at 400 °C for 12 h under vacuum (10^{-2} mbar), then the insertion was carried out in a rotating oven at 130 °C for 24 h. The samples were left another 6 h in the oven at 140 °C to insure a homogenous distribution of the dye molecules in the zeolite channels. With this method, samples of different fluorenone concentrations can be prepared with a maximum loading of up to 1.1 molecules per unit cell. For the electronic spectroscopy measurements, samples with lower loadings (e.g., 0.15 molecules per u.c.) are advantageous because of saturation effects, while for the vibrational spectroscopy measurements, samples with higher loading (e.g., 0.5 molecules per u.c.) are favored.

Physical characterization

Washing of fluorenone/zeolite L with 1-butanol: To remove the dye molecules on the zeolite surface, the following washing procedure was used. In a glove box, dry fluorenone/zeolite L (10 mg) was filled in a weighed 10 mL volumetric flask equipped with magnetic stirrer and septum. 1-Butanol (10 mL) was then introduced through the septum by a syringe. The suspension was put in an ultrasonic bath for several minutes, and then stirred at room temperature for 24 h before being centrifuged (15 min, 4000 rpm). The fluorenone concentration in the supernatant was determined spectrometrically. The same method was applied to rehydrated fluorenone/zeolite L material. Rehydration of fluorenone/zeolite L took place in air of 18–22% relative humidity at room temperature for 24 h.

Determination of fluorenone loading: The effective loading of washed fluorenone/zeolite L samples was determined by dissolving the zeolite framework in an aqueous solution of hydrogen fluoride (8% HF). The fluorenone concentration was determined spectrometrically.

Thermal analysis: The composition of a typical sample was determined by means of TGA. Thermogravimetric measurements were performed on a Mettler Thermobalance TG50. Rehydrated fluorenone/zeolite L (15 mg) was put into a 70 μL aluminum oxide crucible, placed in the thermobalance, and heated in an N_2 stream (ca. 15 mL min^{-1}) from 25 to 900 °C at a rate of 5 °C min^{-1}. Reference measurements for pure zeolite L and crystalline fluorenone were performed following the same method.

Differential scanning calorimetry (DSC): DSC measurements were performed on a Mettler Toledo DSC 822^e. In a typical experiment, rehydrated fluorenone/zeolite L (1 mg) was heated in a sealed aluminum crucible from 35 to 600 °C at a rate of 10 °C min^{-1}, and an N_2 stream of 80 mL min^{-1}. Reference measurements for pure zeolite L and crystalline fluorenone were performed following the same method.

X-ray powder diffraction: The data collection from the unloaded zeolite and the fluorenone/zeolite L samples was performed using a STOE automated powder diffractometer system (Debye–Scherrer scan mode, with small position sensitive detector). A 0.5 mm capillary was used as a sample holder. The observed 2θ range went from 0 to 120°, with a step of 0.02° and a time per step of 1800 s.

Electronic spectroscopy

UV-visible: The absorption spectra were recorded on a Perkin Elmer Lambda 900 UV/VIS/NIR spectrometer. Fluorenone was dissolved in cyclohexane (~10^{-5} M). Quartz cuvettes were used.

Luminescence spectra: The emission and excitation spectra were recorded on a Perkin Elmer LS 50 B luminescence spectrometer. Fluorenone was measured either in solution (cyclohexane, ~10^{-5} M) in quartz cuvettes, or incorporated in zeolite L as thin layers on quartz plates (ϕ1.6 cm). The layers were prepared by suspending fluorenone/zeolite L in 1-butanol (~1 mg in 300 μL), 100 μL of which was placed on a plate, and the solvent evaporated.

Time-resolved spectra: Time-resolved spectra of fluorenone in cyclohexane (~10^{-5} M) and fluorenone/zeolite L were recorded on a Perkin Elmer LS 50 B luminescence spectrometer. Quartz cuvettes were used for solutions, whereas fluorenone/zeolite L was measured as thin layers on quartz plates. The layers were prepared in the same way as described above. Solutions were degassed by three freeze-pump-thaw cycles, while

fluorenone/zeolite L samples were measured in the presence of air. Spectra were recorded at room temperature and at 80 K.

Vibrational spectroscopy

IR spectra: The IR spectra were measured on a BOMEM DA8 FTIR spectrometer equipped with a liquid-nitrogen-cooled MCT detector (500–5000 cm^{-1}) and a KBr beam splitter. All spectra were taken in a high-vacuum cell (2×10^{-5} mbar) with a resolution of 8 cm^{-1}. All fluorenone/zeolite L and zeolite L samples were measured as thin layers coated on ZnSe plates (ϕ8 mm). The layers were typically prepared by suspending about 1 mg of the fluorenone/zeolite L sample in 500 μL of 1-butanol. 45 μL of such a suspension were placed on a ZnSe plate and left to dry.

Raman spectra: The FT-Raman spectra were measured with the Raman accessory of the BOMEM DA8. The spectrometer was equipped with a liquid-nitrogen-cooled InGaAs detector and a quartz beam splitter. A continuous-wave, diode-pumped, Nd^{3+}:YAG laser (Coherent Compass 1064–2500 mn) was used as the excitation beam. Rayleigh scattering was removed by two holographic super notch filters (Kaiser Optical Systems HSPF-1064.0-1.0) in 0° position. All Raman spectra were measured with a resolution of 8 cm^{-1}. Duran glass capillaries served as sample holders for both crystalline fluorenone and fluorenone/zeolite L samples.

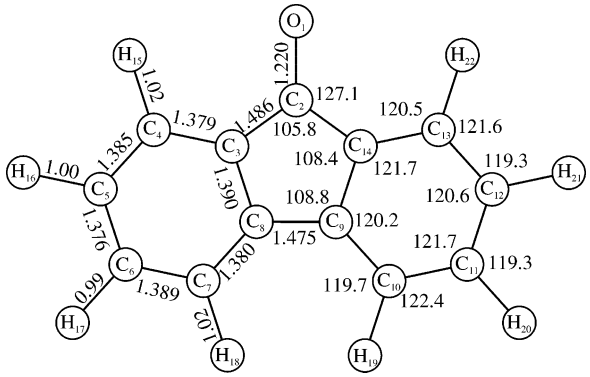

Figure 18. Bond lengths (Å) and angles (°) for fluorenone (C_{2v} symmetry).[6]

Molecular Orbital Calculations

Molecular orbitals: Molecular orbitals (MO) were investigated by means of the extended Hückel molecular orbitals method (EHMO).[39] MO and *EDiT* (*Electronic Dipole-induced Transition*) were calculated using ICONC-EDiT.[40] Off-diagonal elements were calculated by the weighted Wolfsberg–Helmholtz formula with a distance-dependent Hückel constant. The parameters used are given in refs. [17,32]. DOL (density of levels) and L-DOL (local density of levels) were calculated as described in refs. [30,31].

Configuration interaction (CI): The PPP (Pariser–Parr–Pople) method was used to calculate the S_n singlet states.[41] 49 (π–π^*) configurations were included in the CI calculations. All parameters were taken from ref. [42].

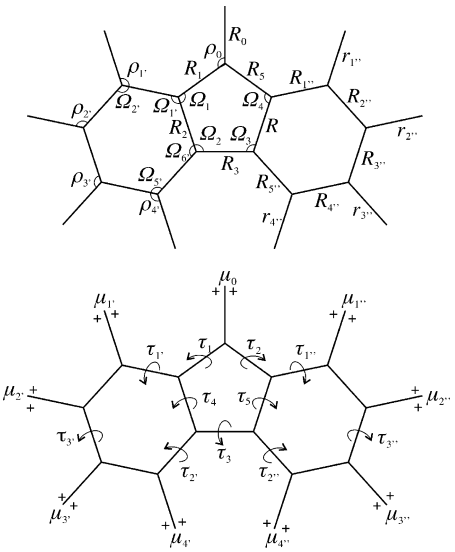

Figure 19. Internal coordinates for fluorenone. Top: in-plane coordinates. Bottom: out-of-plane coordinates.

Normal coordinate analysis: The vibrational analysis was performed by using the Wilson GF matrix method with the extended computer program package QCMP0676 used in ref. [43]. The values for the bond lengths and angles shown in Figure 18 were taken from ref. [6]. They correspond to the average values from an X-ray diffraction analysis of fluorenone. Molecular symmetry was taken as C_{2v} and the molecule was placed in the *xz* plane. Figure 19 shows the numbering of the internal coordinates and Table 6 summarizes the symmetry coordinates used for the normal coordinate analysis.

Table 6. Symmetry coordinates used for the normal coordinate analysis.

			A_1		
S_1	R_0	S_9	$R_{5'}+R_{5''}$	S_{17}	$\Omega_{6'}+\Omega_{6''}$
S_2	R_1+R_5	S_{10}	$r_{1'}+r_{1''}$	S_{18}	$\Omega_{5'}+\Omega_{5''}$
S_3	R_2+R_4	S_{11}	$r_{2'}+r_{2''}$	S_{19}	$\rho_{1'}+\rho_{1''}$
S_4	R_3	S_{12}	$r_{3'}+r_{3''}$	S_{20}	$\rho_{2'}+\rho_{2''}$
S_5	$R_{1'}+R_{1''}$	S_{13}	$r_{4'}+r_{4''}$	S_{21}	$\rho_{3'}+\rho_{3''}$
S_6	$R_{2'}+R_{2''}$	S_{14}	$\Omega_1+\Omega_4$	S_{22}	$\rho_{4'}+\rho_{4''}$
S_7	$R_{3'}+R_{3''}$	S_{15}	$\Omega_2+\Omega_3$	S_{23}	$\rho_{O1}+\rho_{O2}$
S_8	$R_{4'}+R_{4''}$	S_{16}	$\Omega_{2'}+\Omega_{2''}$	S_{24}	$\Omega_{1'}+\Omega_{1''}$
			B_1		
S_{25}	R_1-R_5	S_{33}	$r_{2'}-r_{2''}$	S_{40}	$\Omega_{5'}-\Omega_{5''}$
S_{26}	R_2-R_4	S_{34}	$r_{3'}-r_{3''}$	S_{41}	$\rho_{1'}-\rho_{1''}$
S_{27}	$R_{1'}-R_{1''}$	S_{35}	$r_{4'}-r_{4''}$	S_{42}	$\rho_{2'}-\rho_{2''}$
S_{28}	$R_{2'}-R_{2''}$	S_{36}	$\Omega_1-\Omega_4$	S_{43}	$\rho_{3'}-\rho_{3''}$
S_{29}	$R_{3'}-R_{3''}$	S_{37}	$\Omega_2-\Omega_3$	S_{44}	$\rho_{4'}-\rho_{4''}$
S_{30}	$R_{4'}-R_{4''}$	S_{38}	$\Omega_{2'}-\Omega_{2''}$	S_{45}	$\rho_{O1}-\rho_{O2}$
S_{31}	$R_{5'}-R_{5''}$	S_{39}	$\Omega_{6'}-\Omega_{6''}$	S_{46}	$\Omega_{1'}-\Omega_{1''}$
S_{32}	$r_{1'}-r_{1''}$				
			A_2		
S_{47}	$\mu_{1'}-\mu_{1''}$	S_{51}	$\tau_1-\tau_2$	S_{54}	$\tau_{2'}-\tau_{2''}$
S_{48}	$\mu_{2'}-\mu_{2''}$	S_{52}	$\tau_4-\tau_5$	S_{55}	$\tau_{3'}-\tau_{3''}$
S_{49}	$\mu_{3'}-\mu_{3''}$	S_{53}	$\tau_{1'}-\tau_{1''}$	S_{56}	τ_3
S_{50}	$\mu_{4'}-\mu_{4''}$				
			B_2		
S_{57}	μ_O	S_{61}	$\mu_{4'}-\mu_{4''}$	S_{64}	$\tau_{1'}-\tau_{1''}$
S_{58}	$\mu_{1'}-\mu_{1''}$	S_{62}	$\tau_1-\tau_2$	S_{65}	$\tau_{2'}-\tau_{2''}$
S_{59}	$\mu_{2'}-\mu_{2''}$	S_{63}	$\tau_2-\tau_4$	S_{66}	$\tau_{3'}-\tau_{3''}$
S_{60}	$\mu_{3'}-\mu_{3''}$				

Acknowledgments

We thank Dr. Stephan Glaus for his help with the MO calculations, Dr. Antonio Currao for useful discussions and for his contributions, and Mrs. Arantzazu Zabala Ruiz for the DSC measurements. We also thank Mrs. Beatrice Frey for the TGA and X-ray powder diffraction measurements. This work was supported by the Swiss National Science Foundation Project NF 2000-06784.02/1.

[1] G. Calzaferri, S. Huber, H. Maas, C. Minkowski, *Angew. Chem.* **2003**, *115*, 3860; *Angew. Chem. Int. Ed.* **2003**, *42*, 3732.
[2] M. Pauchard, A. Devaux, G. Calzaferri, *Chem. Eur. J.* **2000**, *6*, 3556.
[3] H. Maas, G. Calzaferri, *Angew. Chem.* **2002**, *114*, 2389; *Angew. Chem. Int. Ed.* **2002**, *41*, 2284.
[4] G. Schultz-Ekloff, D. Wöhrle, B. VanDuffel, R. A. Schoonheydt, *Microporous Mesoporous Mater.* **2002**, 51, 91.
[5] S. J. Hashimoto, *J. Photochem. Photobiol. C* **2003**, *4*, 19.
[6] H. R. Luss, D. L. Smith, *Acta Crystallogr.* **1972**, *28*, 884.
[7] A. Kuboyama, *Chem. Phys. Lett.* **1976**, *41*, 544.
[8] S. Arathi Rani, J. Sobhanadri, T. A. Prasada Rao, *Spectrochim. Acta* **1995**, *51*, 2473.
[9] R. A. Caldwell, *Tetrahedron Lett.* **1969**, *26*, 2121.
[10] T. Kobayashi, S. Nagakura, *Chem. Phys. Lett.* **1976**, *43*, 429.
[11] L. J. Andrews, A. Deroulede, H. Linschitz, *J. Phys. Chem.* **1978**, *82*, 2304.
[12] L. Biczók, T. Bérces, *J. Phys. Chem.* **1988**, *92*, 3842.
[13] B. M. Monroe, R. P. Groff, *Tetrahedron Lett.* **1964**, *10*, 3955.
[14] L. A. Singer, *Tetrahedron Lett.* **1969**, *12*, 923.
[15] K. Yoshihara, D. R. Kearns, *J. Chem. Phys.* **1966**, *45*, 1991.
[16] G. Calzaferri, R. Rytz, *J. Phys. Chem.* **1995**, *99*, 12141.
[17] R. Seifert, R. Rytz, G. Calzaferri, *J. Phys. Chem. A* **2000**, *104*, 7473.
[18] A. K. Aboul-Gheit, M. A. Al-Hajjaji, A. M. Summan, S. M. Abdel-Hamid, *Thermochim. Acta* **1988**, *126*, 397.
[19] A. K. Aboul-Gheit, M. F. Menoufy, *Thermochim. Acta* **1990**, *160*, 193–200.
[20] B. Hennessy, S. Megelski, C. Marcolli, V. Shklover, C. Bärlocher, G. Calzaferri, *J. Phys. Chem. B* **1999**, *103*, 3340.
[21] R. Zwarich, A. Bree, V. Vilkos, *J. Mol. Spectrosc.* **1974**, *51*, 38.
[22] M. Bärtsch, P. Bornhauser, G. Calzaferri, R. Imhof, *J. Phys. Chem.* **1994**, *98*, 2817.
[23] E. M. Flanigen, H. Khatami, H. A. Szymanski, *Adv. Chem. Ser.* **1971**, *101*, 201.
[24] P. Pichat, C. Franco-Parra, D. Barthomeuf, *J. Chem. Soc. Faraday Trans. 1* **1975**, *71*, 991.
[25] K. Tai No, D. H. Bae, M. S. Jhon, *J. Phys. Chem.* **1986**, *90*, 1772.
[26] C. L. Angeli, *J. Phys. Chem.* **1973**, *77*, 222.
[27] E. Castellucci, P. Manzelli, B. Fortunato, E. Gallinella, P. Mirone, *Spectrochim. Acta* **1975**, *31*, 451.
[28] P. C. Painter, R. W. Snyder, *Spectrochim. Acta* **1980**, *36*, 337.
[29] J. D. Head, A. R. Mitchell, L. Noodelman, *Surf. Sci.* **1977**, *69*, 714.
[30] S. Megelski, A. Lieb, M. Pauchard, A. Drechsler, S. Glaus, C. Debus A. J. Meixner, G. Calzaferri, *J. Phys. Chem. B* **2001**, *105*, 25.
[31] S. Glaus, G. Calzaferri, R. Hoffman, *Chem. Eur. J.* **2002**, *8*, 1785.
[32] D. Brühwiler, N. Gfeller, G. Calzaferri, *J. Phys. Chem. B* **1998**, *102*, 2923.
[33] J. A. van Bokhoven, M. J. van der Eerden, D. C. Koningsberger, *J. Am. Chem. Soc.* **2003**, *125*, 7435.
[34] B. G. Silbernagel, A. R. Garcia, J. M. Newsam, R. Hulme, *J. Phys. Chem.* **1989**, *93*, 6506.
[35] B. L. Su, *J. Chem. Soc. Faraday Trans.* **1997**, *93*, 1449.
[36] B. L. Su, V. Norberg, C. Hansenne, *Langmuir* **2000**, *16*, 1132.
[37] C. Hansenne, F. Jousse, L. Leherte, D. P. Vercauteren, *J. Mol. Catal.* **2001**, *166*, 147.
[38] S. Megelski, G. Calzaferri, *Adv. Funct. Mater.* **2001**, *11*, 277
[39] R. Hoffmann, *J. Chem. Phys.* **1963**, *39*, 1397.
[40] G. Calzaferri, R. Rytz, M. Brändle, D. Brühwiler, S. Glaus, *ICON-EDiT, Extended-Hückel Molecular Orbital and Electronic Dipole-induced Transition Calculations*; available at http://dcbwww.unibe.ch/groups/calzaferri/start.html, update **2000**.
[41] a) R. Pariser, R. G. Parr, *J. Chem. Phys.* **1953**, *21*, 466; b) R. Pariser, R. G. Parr, *J. Chem. Phys.* **1953**, *21*, 767; c) J. A. Pople, *Trans. Faraday Soc.* **1953**, *49*, 1375.
[42] J. Fabian, A. Mehlhorn, R. Zahradník, *Theor. Chim. Acta* **1968**, *12*, 247.
[43] C. Marcolli, G. Calzaferri, *J. Phys. Chem. B* **1997**, *101*, 4925.

Received: October 30, 2003 [F5673]

Published online: March 25, 2004